

A KECK HIRES INVESTIGATION OF THE METAL ABUNDANCES AND KINEMATICS OF THE $z = 2.46$ DAMPED $\text{Ly}\alpha$ SYSTEM TOWARD Q0201+365

JASON X. PROCHASKA & ARTHUR M. WOLFE¹

Department of Physics, and Center for Astrophysics and Space Sciences;
University of California, San Diego;
C-0111; La Jolla; CA 92093

ABSTRACT

We present high resolution ($\approx 8 \text{ km s}^{-1}$) spectra of the QSO Q0201+365 obtained with HIRES, the echelle spectrograph on the 10m W.M. Keck Telescope. Although we identify over 80% of the absorption features and analyze several of the more complex metal-line systems, we focus our analysis on the damped $\text{Ly}\alpha$ system at $z = 2.462$. Ionization simulations suggest the hydrogen in this system is significantly neutral and all of the observed metals are predominantly singly ionized. We measure accurate abundances for Fe, Cr, Si, Ni and place a lower limit on the abundance of Zn: $[\text{Fe}/\text{H}] = -0.830 \pm 0.051$, $[\text{Cr}/\text{H}] = -0.902 \pm 0.064$, $[\text{Si}/\text{H}] = -0.376 \pm 0.052$, $[\text{Ni}/\text{H}] = -1.002 \pm 0.054$ and $[\text{Zn}/\text{H}] > -0.562 \pm 0.064$. We give evidence suggesting the actual Zn abundance is $[\text{Zn}/\text{H}] \approx -0.262$, implying the highest metallicity observed at a redshift $z \geq 2$. The relative abundances of these elements remains constant over essentially the entire system ($\approx 150 \text{ km s}^{-1}$ in velocity space), suggesting it is well mixed. Furthermore, we use the lack of abundance variations to infer properties of the dust responsible for element depletion. Finally, we discuss the kinematic characteristics of this damped $\text{Ly}\alpha$ system, comparing and contrasting it with other systems. The low-ion line profiles span $\approx 200 \text{ km s}^{-1}$ in velocity space and have an asymmetric shape with the strongest feature on the red edge. These kinematic characteristics are consistent with a rotating disk model.

Subject headings: galaxies: evolution—galaxies: formation—quasars: quasars—absorption lines—quasars: individual (Q0201+365)—galaxies: abundances

¹Visiting Astronomer, W.M. Keck Telescope. The Keck Observatory is a joint facility of the University of California and the California Institute of Technology.

1. INTRODUCTION

This paper is the second in a series devoted to studying the metal content of high-redshift galaxies and their progenitors. Our primary objectives are

- (1) to record the emergence of metals in galaxies,
- (2) to trace the mean cosmic metallicity from $z \approx 4.5$ to the present,
- (3) to determine the kinematic state of galaxies from $z \approx 4.5$ to the present.

We are implementing this study using HIRES, the echelle spectrograph on the Keck 10m telescope (Vogt 1992), to obtain high-resolution spectra of QSOs with foreground damped Ly α systems. The damped Ly α systems are a population of neutral gas layers exhibiting properties indicating they are either galaxy progenitors, or well formed galaxies detected during an early evolutionary phase. Recent studies indicate the comoving density of neutral gas in damped systems at $z \approx 3.3$ is comparable to the density of visible stars in current galaxies. At lower redshifts, the comoving density of neutral gas decreases with time in a manner consistent with gas consumption by star formation (Wolfe et al. 1995). Therefore, studies of the metal content of the damped Ly α systems enable one to trace the chemical evolution of representative galaxies from a presumably metal-poor gaseous progenitor phase to metal rich epochs when most of the baryons are in stars. As a result, the age-metallicity relation, kinematic conditions, etc., deduced from the damped Ly α systems should tell us more about the history of galaxies at large redshifts than analogous relations deduced from old stars found in the solar neighborhood (Evardsson et al. 1993).

In a previous paper we presented echelle spectra of the $z = 2.309$ damped system toward PHL 957 at a spectral resolution of $\approx 8 \text{ km s}^{-1}$ (FWHM) and signal-to-noise ratio of $\approx 35:1$ (Wolfe et al. 1994). By fitting multiple Voigt velocity components to low-ion transitions such as Zn II 2026, Ni II 1741, and Cr II 2062 we obtained accurate abundances for Zn, Ni, and Cr in the neutral gas. The Zn and Cr abundances were accurate because we resolved Zn II 2062.664 from Cr II 2062.234 for the first time in a QSO absorption system. We found that the abundances relative to solar were low: $[\text{Zn}/\text{H}] = -1.55 \pm 0.11$, $[\text{Cr}/\text{H}] = -1.79 \pm 0.10$, and $[\text{Ni}/\text{H}] = -2.13 \pm 0.08$. The Zn abundance is especially significant because Zn is relatively undepleted by grains in the ISM of the Galaxy (Sembach et al. 1995) and is presumably unaffected by dust which may be present in damped Ly α systems (Fall and Pei 1993). We also found the line profiles to be asymmetric in the sense that the low column density gas was found in absorption only at velocities higher than the high column-density gas. The kinematics can be explained by the passage of the line of sight through a rotating disk in which the density of clouds decreases with radius and with perpendicular distance from midplane.

The purpose of this paper is to present HIRES spectra for Q0201+365, a $V = 17.5$ QSO with emission redshift $z_{em} = 2.49$. While we identify more than 80% of the absorption features and find a total of 13 metal-line redshift complexes, the focus of this paper is on the damped Ly α system at $z = 2.462$ (Lanzetta et al. 1991, Lu et al. 1993). Lu et al. 1993 studied this system at a resolution of $\approx 50 \text{ km s}^{-1}$. They fitted a Voigt damping profile to the Ly α absorption trough and found $N(\text{HI}) = 2.4 \times 10^{20} \text{ cm}^{-2}$. They also identified the metal transitions Si II 1190, Si II 1193, Si III 1206, Si II 1260, and Fe II 1144. Because these transitions are (a) saturated and (b) in the Ly α forest, neither the abundances nor kinematics were accurately measured. The present study represents a major improvement over the previous work for the following reasons. First, we obtain spectra at a resolution of $\approx 8 \text{ km s}^{-1}$ and a typical signal-to-noise ratio of 33:1. Second, in contrast to the previous work, we focus on metal lines redward of Ly α emission where confusion with Ly α forest lines is absent. Third, because of the higher accuracy of the data we focus on weak unsaturated transitions of ions expected to dominate the ionization state of gas in neutral clouds. In fact we establish accurate element abundances for Fe, Si, Ni, and Cr, and a lower limit on the abundance of Zn. Furthermore, we use computer simulations to investigate the ionization of this system. We also analyze the relative metal abundances and comment on the characteristics of dust grains in this system. In addition, we examine a Ly α absorption system at $z = 1.955$ and use kinematic and abundance arguments to suggest it may be a damped Ly α system. Finally, we discuss the kinematics of the $z=2.462$ damped absorption system, contrasting its features with several other systems toward Q0201+365, as well as other damped Ly α systems measured with HIRES (Wolfe et al. 1994).

The paper is organized as follows. In § 2 we describe the data acquisition and reduction techniques, present the spectra (Figure 1) and give a nearly complete absorption line list in Table 2. We detail the analytic methods utilized throughout the paper in § 3. In § 4 we present velocity profiles of the most significant metal line systems along with the VPFIT package solutions where applicable. § 5 presents the ionic column densities of the two systems associated with the damped Ly α profile at $z=2.46$. In § 6 we argue that the degree of photoionization of the damped Ly α system is low. § 7 gives the results of the abundance measurements and discusses the possible depletion of the gas-phase metals by dust grains. We also describe the kinematics of the Ly α system. Finally, § 8 summarizes the results and gives concluding remarks.

2. DATA

In this section we present the HIRES spectra, detailing the techniques used for the acquisition and reduction of the data. Table 2 gives an absorption line list with measured equivalent widths and 1σ errors and identifies over 80% ($\geq 88\%$ redward of the Ly α forest) of the features.

2.1. Acquisition

We observed Q0201+365 with the HIRES echelle spectrograph on the 10m W.M. Keck Telescope on three separate nights for a total integration time of 9.7 hrs. Table 1 presents a journal of the observation dates, exposure times, wavelength coverages and resolution of the data. Unfortunately, the signal to noise ratio (SNR) of the data was significantly limited by clouds. We used the kv38 filter to block out 2nd order blue wavelengths, the C5 decker plate with 1.1" slit, and standard 2×1 binning on the 2048 x 2048 Tektronix CCD. This setup afforded a resolution ranging from 7.2 – 8.0 km s $^{-1}$ and wavelength coverage from 4720 – 7180 Å over 26 orders. Gaps are evident between orders redward of ≈ 5100 Å where the free spectral range of the echelle exceeds the format of the CCD. For reduction and calibration we took 300s exposures of the nearby standard star BD+28411 and images of quartz and Th-Ar arc lamps.

2.2. Reduction

The 2-D CCD images were reduced to 1-D uncalibrated spectra with a software package kindly provided by T. Barlow (1995). In short, the package subtracts the baseline and bias from the 2-D frames, determines the gain from dark images converting digital numbers (DN) to e $^{-}$ counts, and extracts the data from the 2-D images by tracing the bright standard-star profile. It also performs sky subtraction and the removal of cosmic ray events.

We wavelength calibrated the data of each night by fitting low-order Legendre polynomials to our Th-Ar arc frames, properly correcting to vacuum heliocentric wavelengths. We obtained continuum fits to the spectra by fitting high-order Legendre polynomials to the spectral flux in each order. The continuum fits were then used to normalize the flux to unity. We also calculated a 1σ error array assuming Poisson statistics, ignoring the errors associated with sky subtraction and continuum fitting (i.e. $\sigma = \sqrt{N_{\text{obj}} + N_{\text{sky}}}$). Finally we coadded the spectra, weighting by the calculated SNR of

each image while rejecting spurious values assumed to arise from cosmic rays or poor sky subtraction. The final average SNR is ≈ 30 with the exception of Order 75 (SNR ≈ 22) where only one night of data was acquired due to a difference in the alignment of the CCD on the first night. The spectra are presented along with 1σ error arrays in Figure 1.

2.3. Absorption Lines

Table 2 lists the wavelengths, equivalent widths and 1σ errors for all absorption line features which exceed the 5σ limit in equivalent width as measured by techniques similar to those of Lanzetta et al. (1991). We believe 5σ is a conservative but appropriate limit for this data. The reported wavelengths represent rough estimates of the centroids of complex line profiles and should be taken only as guides for differentiating between features. Because almost all of the transitions are resolved, an accurate determination of the wavelength of every feature would require months of laborious Voigt profile fitting. This task bears little scientific merit for the task of the present paper which is to examine specific systems. For this reason, we carried out detailed profile fits for only a selected subset of the lines in Table 2. We do not report equivalent widths for those features identified as sky absorption lines or complicated multi-system blends.

Table 2 also includes the transition names and approximate redshifts of those features we successfully identified. Identification proceeds in a largely *ad hoc* fashion, with the initial emphasis placed on finding C IV and Si IV doublets. Once we composed a list of redshifts for the metal-line systems, we attempted to match the remaining features with the strongest metal-line transitions. Finally, we compared the line profiles of the transitions of a given redshift system in velocity space for conclusive identification. Although fairly laborious, this approach is highly effective and essentially error-proof.

By comparing the object frames with the similarly reduced standard star images, we identified night-sky emission and absorption features in the spectra. These features are labeled appropriately in Table 2 along with all other identified spurious features.

Table 3 lists the rest wavelengths and oscillator strengths for all of the metal transitions analyzed in this paper. Almost all of the values are taken from Morton (1991). It is important to be very clear what values are assumed in order to allow for consistent abundance comparisons.

3. ANALYTIC METHODS

This section describes the least squares line profile fitting method and the apparent optical depth method used to analyze our metal line systems.

3.1. VPFIT (Least-Squares Line-Profile Fitting Method)

With the aid of the VPFIT fitting package kindly provided by R.F. Carswell we performed least-squares fits of Voigt profiles, produced by individual Gaussian components, to our metal lines for several of the absorption systems toward Q0201+365. The VPFIT package fits Voigt profiles to an absorption system, simultaneously determining the redshift, column density, b values (where the Doppler velocity b and velocity dispersion σ are related by $b = \sqrt{2}\sigma$) and associated errors of the individual components while minimizing a χ^2 parameter matrix. When performing a fit, one can tie several transitions together forcing the redshift and b values of the different transitions to match while allowing the column densities to vary individually.

In performing the fits we first isolated the broadest resolved transition in a given absorption complex. We found we could always obtain a reasonably accurate profile fit to this transition. We then tied it together with the other associated transitions. Given the inherent differences between low and high-ion line profiles, we chose to treat the two types separately. If necessary, we added or removed a velocity component to those transitions with line profiles that have features not evident in the other transitions. In several cases, this significantly lowered the final χ^2 value. In all our fits we assumed bulk motion dominates thermal motion because damped Ly α systems are relatively cool ($T < 1000$ K) and the transitions arise in metals that are comparatively massive. We also set a minimum value for the b parameter at 3 km s^{-1} to prevent the package from fitting features narrower than ≈ 4 pixels, the FWHM of the line spread function.

3.2. Apparent Optical Depth Method and Hidden Component Analysis

Savage and Sembach (1991) have stressed that measuring column densities with the line profile method does not always account for hidden saturated components. These saturated components may be under represented in the line profile analysis, leading to significant errors in the measured ionic column densities. Therefore, as a check on our VPFIT results we performed a hidden component analysis of those ions where multiple transitions were observed (e.g. Ni⁺ for the damped Ly α system at $z = 2.462$). The analysis

involves calculating $N_a(v)$, the apparent column density per unit velocity, for each pixel from the optical depth equation

$$N_a(v) = \frac{m_e c \tau_a(v)}{\pi e^2 f \lambda}, \quad (1)$$

where $\tau_a(v) = \ln[I_i(v)/I_a(v)]$, f is the oscillator strength, λ is the rest wavelength and I_i and I_a are the incident and measured intensity. Comparing $N_a(v)$ deduced from two or more transitions of the same ion, one finds the stronger transition will have smaller values of $N_a(v)$ in those features where hidden saturation is present. Thus, one can ascertain the likelihood of saturated components for ions with multiple transitions. Furthermore, summing $N_a(v)$ over the proper velocity intervals serves as an excellent check on ionic column densities measured with the VPFIT package, and as a further check on the existence of saturation.

4. VELOCITY PLOTS AND VPFIT SOLUTIONS

This section presents the velocity profiles of the most complex metal line absorption systems toward Q0201+365. For several of the systems, we superimpose the solutions of our least square fits from the VPFIT package. In all plots a dashed vertical line is drawn for reference, usually identifying the strongest feature present. For clarity, we have plotted features not related to the given system with dotted lines.

4.1. Damped Ly α System ($z = 2.462$)

Figure 2 presents the line profiles and fits of the transitions associated with the damped Ly α system at $z=2.462$ ². The velocity centroids for the Gaussian components of the fit to the low-ion profiles are denoted by the short vertical lines above the Fe II 1608 profile. The velocity centroids for the high-ion fits are the vertical lines above the Si IV 1393 profile. We found 13 individual components were required for an optimal fit to the low-ions. The multi-component fit to the transitions Fe II 1608, Ni II 1741, Ni II 1751, Cr II 2056 and Si II 1808 has a reduced $\chi^2_\nu = 1.05$ with a probability $P_{\chi^2} = 0.216$. Table 4a lists the redshift, b value and column density along with 1σ error of every velocity component in the VPFIT

² Note there are two ‘subsystems’ within the velocity space of the damped Ly α profile: the present subsystem and the $z=2.457$ subsystem discussed in §4.2

solution. The quality of the fit reflects the high degree to which the low-ion profiles track one another.

On the other hand, 10 components (only 8 over the same region as the low ion profiles) were necessary for an optimal fit to the high-ion transitions C IV 1550 and Si IV 1393. These components are significantly broader (higher b values) than those of the low-ions. This fit is not as accurate as the low-ion fit ($\chi^2_\nu = 1.805$) because it is much more difficult to fit broad shallow components such as those around $\approx -260 \text{ km s}^{-1}$. The results of this fit are presented in Table 4b.

Figure 3 shows velocity profiles of 4 transitions we chose not to fit with the VPFIT package. Because the Al II 1670 profile is so highly saturated, we were unable to accurately fit it with the other low-ion profiles. In particular, the VPFIT package could not properly model the heavy absorption at $\approx -140 \text{ km s}^{-1}$. The Al III 1862 profile exhibits characteristics of both the low and high-ion transitions and therefore was difficult to fit to either. Instead, we measured its column density with the apparent optical depth method. Finally, the 3 transitions Zn II 2026, Cr II 2062 and Zn II 2062 all suffer from significant blending: Zn II 2026 is blended with both Fe II 2374 and Fe II 2600 from 2 other systems, and Zn II 2062 and Cr II 2062 are blended with each other. As a result all three transitions were excluded from the fit.

4.2. Companion System at $z=2.457$

The velocity profiles and least-square fits of the other subsystem (found at $z=2.457$) associated with the damped Ly α system at $z=2.46$ is shown in Figure 4. A 12 component fit to the low-ion transitions Fe II 1608, Si II 1526 and Al II 1670 was optimal and yielded a reduced $\chi^2_\nu = 1.50$. Difficulties arose in fitting the Fe II 1608 profile because the second component appears to have a significantly lower b value than the same component in the other low-ion profiles. This may be a result of thermal broadening. We also fitted the high-ions SiIV 1393, 1402 and CIV 1548 and again found broader, fewer components were required in the best fit. Tables 5a and 5b list the results of the fits.

4.3. Possible Damped System at $z=1.955$

Figure 5 presents the velocity profiles for a redshift system with $z=1.955$ which is a possible damped Ly α system. We chose not to fit this system because significant blending with other systems prevented us from determining which features are associated only

with the $z=1.955$ system. In particular, we have been unable to determine whether the absorption seen at positive relative velocities in Figure 5 is due to the $z=1.955$ system.

Lu et al. (1994) could not confidently classify the system as damped because the noisy Ly α profile could not be fitted with a Voigt damping profile. The metal lines have many resolved components and exhibit a large velocity interval ($\approx 250 \text{ km s}^{-1}$). Figure 6 plots the observed Ly α profile, a Voigt damped Ly α profile, and the Fe II 1608 line profile. The Voigt Ly α profile was derived by letting $N(\text{HI}) = 1.5 \times 10^{20} \text{ cm}^{-2}$ at $z=1.955$. It appears the low-ions satisfy the metal criteria associated with damped Ly α systems; i.e., the low-ion metal profile is significantly narrower than the Ly α profile and its velocity centroid is near that of the Ly α profile (Wolfe et al. 1993). An apparent optical depth measurement of the Cr II and Si II ions gives $N(\text{Cr}^+) = 12.73 \pm .070$ and $N(\text{Si}^+) = 15.25 \pm 0.03$ suggesting a lower limit of $\log[N(\text{H})] \geq 19.0$ and 19.7 respectively, assuming cosmic abundances and no dust depletion. This analysis indicates the $z=1.955$ system may be damped. Furthermore, Figure 5 reveals evidence for C I 1656, a transition previously seen only in damped Ly α systems. However, even with our high resolution data the proper classification remains inconclusive.

4.4. System at $z=2.325$

The velocity profiles and VPFIT profile solutions for the absorption system at $z=2.325$ are shown in Figure 7. Note the feature at -80 km s^{-1} in the CIV 1548 transition is due to a blend with the CIV 1550 transition from the system at $z=2.320$. By contrast with the damped system, the Al III 1854 transition was best fitted with the low-ion solution. We tied the Si II 1526, Fe II 1608, Al II 1670, and Al III 1854 transitions together and fitted the CIV doublet separately. Tables 6a and 6b present the results of the 2 fits. Unlike the damped system, the high and intermediate ions more closely follow the low-ion profiles. Because the high-ion profiles have several components with higher b values, however, it is still impossible to fit them together.

Figure 8 plots the Si II 1526, C IV 1550 and Ly α profiles for the $z=2.325$ system. All three transitions span nearly the same velocity interval and track one another moderately well. As expected the Ly α profile tracks the low-ion profiles (in particular the component at $v \approx 20 \text{ km s}^{-1}$) more closely than the high-ion profiles. Although we did not fit the Ly α profile, Figure 8 is consistent with the profiles of Lyman limit systems.

4.5. Mg II Systems at $z=1.476$, 1.699

Figure 9 shows the velocity profiles of two Fe II and Mg II transitions for metal line systems found at the redshifts $z=1.476$ (a) and $z=1.699$ (b). Both sets of transitions are relatively complex and most of the absorption spans moderate velocity intervals ($\approx 100 \text{ km s}^{-1}$). However, the Fe II 2374 and Fe II 2586 transitions in the $z = 1.476$ system may exhibit an additional feature at $\approx -275 \text{ km s}^{-1}$. Because the predicted wavelengths for the other Fe II lines fall in the inter order gaps, we cannot verify the reality of this feature.

Figures 10a and 10b are hidden component analyses of the Fe transitions from the two systems. Fe II 2586 was not plotted in either hidden component analysis because it closely traces the Fe II 2374 profile in each system and would clutter the figures. In Figure 10a, the weakest Fe transition (Fe II 2374) has significantly larger $N_a(v)$ values, while the strongest Fe transition (Fe II 2600) has the smallest $N_a(v)$ profile. This is direct evidence of hidden saturated components. In fact, because of these hidden components, we found it impossible to fit all of the transitions together in the $z=1.476$ system. We were successful in fitting the Fe II 2344, 2586 transitions, however, and the results are presented in Table 7.

There is little evidence of hidden saturated components in the $z=1.699$ system. What the hidden component analysis does reveal, however, is a blend in the Fe II 2374 profile with Al III 1854 from the $z = 2.457$ at velocities greater than $\approx 0 \text{ km s}^{-1}$ and a blend in the Fe II 2600 profile with Fe II 2374 from the $z = 1.955$ system at velocities lower than $\approx -70 \text{ km s}^{-1}$. Unfortunately, these blends, and the low SNR in the Fe II 2586 and Fe II 2374 profiles prevented accurate profile fits.

5. IONIC COLUMN DENSITIES

This section presents the ionic column densities of the two systems associated with the damped Ly α profile at $z = 2.46$. We perform hidden component analyses where applicable, and use both the line profile and apparent optical depth methods to measure column densities.

5.1. Damped Ly α System at $z = 2.462$

The hidden component analysis of the Ni II 1741, 1751 transitions for the damped Ly α system at $z = 2.462$ is shown in Figure 11. With a few minor exceptions, the $N_a(v)$ curves for the two Ni II transitions match within 1σ , suggesting no hidden saturated

components. Therefore, abundances based on column densities inferred from profile fitting or the apparent optical depth method should not suffer from significant hidden saturation effects. Table 8 lists the measured ionic column densities and 1σ errors for Fe^+ , Cr^+ , Si^+ , Al^+ and Ni^+ for the damped Ly α system at $z=2.462$ as measured by both the line profile (VPFIT) and apparent optical depth methods. For the line profile method we summed the column densities of the individual components of each transition and calculated the 1σ error in the total value with standard least squares techniques.

We adopt a final value for the ionic column density for all of our measurements by averaging the two values and adopting the VPFIT errors. We found the apparent optical depth method underestimates the error, particularly transitions which are nearly saturated (e.g. FeII 1608). For nearly saturated or very weak lines, errors associated with sky subtraction and continuum fitting will play a significant role, yet these errors are not included in the 1σ array. The VPFIT package estimates errors based on the fit of all profiles and is influenced more by the deviation of the data from the fit. Therefore, we chose to adopt the VPFIT errors for all of the ions. Note that in almost every case the calculated values from the two methods match, further indicating no hidden saturated components.

As noted above, we can place only a lower limit on the Zn^+ column density because of blending. We find the Zn II 2026 transition to be dominated by Fe II 2374 associated with the $z = 1.955$ absorption system, and Zn II 2062 to be partially blended with the stronger Cr II 2062 transition. Although Zn II 2026 cannot be extracted from the Fe II profile, the Zn II 2062 profile can be used to estimate a lower limit on the Zn^+ abundance. Figure 12 is a hidden component analysis of the Cr II 2056 and Cr II 2062 transitions. Note that the Cr II 2062 (dotted) profile dominates the Cr II 2056 profile over the entire velocity interval, as expected if Zn II 2062 is present. This analysis reveals two features around 40 and 60 km s^{-1} evident only in the Cr II 2062 profile. We suggest that these two components are not due to Cr^+ absorption, but are components of Zn II 2062 at the high velocity edge of the profile. In the velocity space of Zn II 2062 these components correspond exactly to the strongest components of the other low-ion profiles at $z=2.46258$ and $z=2.46280$ (i.e. at $v = -20$ and 0 km s^{-1} in the Zn II velocity space). Our hidden component analysis of Cr II reveals a third component of Zn II at 7139.66 \AA (-60 km s^{-1} in Figure 12), also corresponding to a significant feature in the other low-ion profiles.

Summing the column densities over velocity space with the apparent optical depth method, we find we find $\log N(\text{Zn}^+)_i = 11.753 \pm 0.116$, 12.087 ± 0.066 , and 12.060 ± 0.074 respectively for the three components (blue to red). The resulting lower limit for the total Zn^+ abundance, $\log N(\text{Zn}^+)_t = 12.468 \pm 0.046$ where the error reported is only useful as an indication of the uncertainty in this lower limit value.

Table 8 also lists ionic column densities for the *s*-process transitions Pb II 1682 and Ge II 1602. Because these transitions are so weak, we used linear curve of growth to infer the column densities from the respective rest-frame equivalent widths. We report the following values for the rest-frame equivalent width of the transitions: $W(\text{Pb}) = 1.78 \pm 0.47 \times 10^{-2} \text{ \AA}$ and $W(\text{Ge}) = -3.4 \pm 4.6 \times 10^{-3} \text{ \AA}$. The negative equivalent width value for Ge II 1602 is certainly a function of the continuum error and is consistent with a null detection (less than even a 1σ detection). We have chosen, therefore, to report its column density and abundance in terms of a 3σ upper limit. The Pb II 1682 value is significant at the 3σ level, but could also be explained through a sizable continuum error, improper sky subtraction, or an unidentified blend. Although Sn II 1400 and Ga II 1414 both lie within our wavelength coverage, they are overwhelmed by blends with transitions from other metal line systems and could not be analyzed.

5.2. Companion Subsystem at $z=2.457$

Table 9 presents the measured ionic column densities for the transitions of the companion system at $z=2.457$. Final values are adopted according to the criteria described above. In nearly all of the low-ion transitions the measured column densities are ≈ 20 times lower than those from the $z=2.462$ subsystem. On the other hand the column densities of the high-ions are nearly the same, possibly indicating this system is in a higher state of ionization, that the two ion groups are kinematically disjoint, or that the same high-ion gas envelopes two dissimilar low-ion configurations.

6. IONIZATION

This section investigates the photoionization of the damped Ly α system at $z=2.462$.

6.1. Ly α Profile

Figure 13 is a velocity plot of the Ly α profile and Fe II 1608 profiles associated with the two absorption systems at $z=2.462$ and $z=2.457$ together with the velocity profile of the Fe II 1608 transitions. Unrelated features at ≈ -800 and 500 km s^{-1} have been removed for clarity. We derived the Voigt profile by distributing the total HI column density, $\log N(\text{H}^0) = 20.38$, into the 23 Fe II 1608 velocity components weighted by their corresponding column density fractions ($N(\text{Fe}^+)_i/N(\text{Fe}^+)_{\text{tot}}$). This treatment is proper provided (a) the Fe II

1608 line profiles accurately trace the HI gas, as one would predict for a sufficiently neutral system, and (b) [Fe/H] is constant across the entire velocity profile, which is predicted for a well mixed system. As Figure 13 demonstrates, the resulting Voigt profile is well fitted to the low resolution data. Table 10 lists the column density, redshift and b values of the 23 components as adopted. Here, about 5% of the HI gas is located in the companion system at $z=2.457$. We found one could place no more than 15% of the HI gas in the companion system before significantly distorting the left wing of the Ly α line profile.

6.2. Ionization Models

6.2.1. Neutral Hydrogen Model

Table 10 shows that all but the most abundant components of our damped system have $\log[N(\text{HI})] \leq 19.5$. If these clouds were isolated structures in the IGM, they would be highly ionized. This would markedly reduce the accuracy of abundance determinations based on the assumption that most of the hydrogen is neutral and most of the metals are singly ionized.

In order to address this problem we ran several ionization simulations with the aid of a program developed by Vincent Virgilio to investigate the predicted neutral hydrogen fraction (H^0 / H) in the damped system. Figure 14a shows the neutral hydrogen fraction plotted against $\log[N(\text{H}^0)]$ measured from either face of a plane-parallel layer with constant H volume density, $n_H = 0.1 \text{ cm}^{-3}$. The layer is subjected on both sides to attenuated power law continuum radiation as calculated by Madau (1992) for a redshift of $z=2.46$ with a mean intensity of $J_\nu = .195 \times 10^{-21} \text{ ergs s}^{-1} \text{ cm}^{-2} \text{ Hz}^{-1} \text{ sr}^{-1}$ at 1 Rydberg. The simulation assumes a temperature of 10^4 K (purely for determining the recombination rate of H^+) while satisfying the ionization and transfer equations in a large number (100) of parallel discrete cells. Each face of the plane parallel layer is illuminated by uniform radiation with incidence angles covering 2π steradians. The calculation also assumes zero source function (i.e. no reemission). Although this model is rather simplified, we find similar CLOUDY (version 84.12: Ferland 1991) calculations are in good agreement with our results. Figure 15 compares the neutral fraction predictions of our model with the corresponding predictions by CLOUDY. The 2-sided illumination simulation predicts a lower neutral fraction than CLOUDY even though CLOUDY assumes only perpendicular incidence. Thus, our simulations reveal that the 1-sided assumptions inherent in CLOUDY are probably underestimating the degree of ionization in optically thick absorption systems.

Our simulations predict a uniform layer with $N(\text{H}^0) = 2.4 \times 10^{20} \text{ cm}^{-2}$ and

$n_H = 0.1 \text{ cm}^{-3}$ will be 96% neutral. The results should be similar for a more realistic multicomponent system, since we expect the majority of the 23 components in the $z=2.46$ system to be shielded from ionizing radiation by gas both above and below the location of the cloud in the layer, thereby maintaining neutrality (Figure 14b). Therefore, we measure the metal abundances of our damped Ly α system by assuming the abundance of element X to equal $N(X^+)/N(\text{H}^0)$, where X^+ is the first ionization state of element X. Note, however, that this result is very dependent on the value of n_H . For instance, we find a neutral fraction of $\approx 37\%$ for $n_H = 10^{-3} \text{ cm}^{-3}$ and $N(\text{H}^0) = 2.4 \times 10^{20} \text{ cm}^{-2}$. Of course, physically this would imply a very large system with dimensions exceeding 100 kpc.

6.2.2. CLOUDY simulations

We have performed CLOUDY photoionization simulations with the aim of using the relative abundances of different ionization states of the same element to estimate the degree of ionization of our system. The analysis parallels the treatment presented by Lu et al. (1995). For the input radiation we used an attenuated power law ionizing spectrum computed by Madau (1992). The spectrum was normalized to a mean intensity of $J_\nu = .195 \times 10^{-21} \text{ ergs s}^{-1} \text{ cm}^{-2} \text{ Hz}^{-1} \text{ sr}^{-1}$ at 1 Rydberg calculated at an average redshift of $z=2.46$. The calculations assume a plane-parallel geometry with only one face illuminated and with incident radiation perpendicular to the surface, in contrast to the more realistic assumptions used to calculate H^0/H in the previous section. The metallicity is fixed at $[\text{Z}/\text{H}] = -0.5$, the hydrogen volume density is varied, and the program terminates at a column density $\log[N(\text{H}^0)] = 20.38$. Thus the neutral hydrogen column density is fixed at the observed value $\log[N(\text{H}^0)] = 20.38$ while the total hydrogen column density is allowed to vary. Although this simulation is overly simplified (e.g. single side illumination, normal incidence, no dust depletion model), it does provide a good estimate of the degree of ionization. Figure 15 presents the results of the simulations. Note that no conclusions concerning the degree of ionization can be drawn by comparing the relative abundances of the low-ions because their column densities track $N(\text{H}^0)$ which is held constant.

Given the CLOUDY results, we can use the observed Si^+ to Si^{3+} and Al^+ to Al^{++} ratios to determine the ionization level of the gas. Since the AlIII profile is heavily saturated, we take $N(v) = 12.00$ per pixel corresponding to $I_a(v)/I_i(v) = 0.05$ in the optical depth equation (Equation 1). Given the degree of saturation, this value yields a *very conservative* lower limit for $[\text{Al}^+/\text{Al}^{++}] \equiv \log[N(\text{Al}^+)] - \log[N(\text{Al}^{++})]$. Figure 17 is a plot of (a) $[\text{Si}^+/\text{Si}^{3+}]$ and (b) $[\text{Al}^+/\text{Al}^{++}]$ for 5 pixel bins over the entire low-ion region. The large dots represent the average value over the velocity regions defined by the vertical dashed lines and

the borders of the plot. Table 11 gives the values of $[\text{Si}^+/\text{Si}^{3+}]$ and $[\text{Al}^+/\text{Al}^{++}]$ as well as the corresponding H^0/H^+ ratio derived from the CLOUDY results for the velocity regions.

With the exception of the region $-40 \text{ km s}^{-1} < v < 40 \text{ km s}^{-1}$, we find $[\text{Al}^+/\text{Al}^{++}] > 0.4$ dex. This yields a neutral hydrogen fraction $\text{H}^0/\text{H} > 0.5$. The velocity region $v = [-100, 40] \text{ km s}^{-1}$ corresponds to the strongest feature in all of the low-ion profiles and we expect the abundance of Al II to greatly exceed the value assumed above. The $[\text{Si}^+/\text{Si}^{3+}]$ results are more difficult to interpret because the Si IV line-profile does not closely trace the low-ion or Al III profiles. According to the SiII to SiIV ratio, the most highly ionized region is $-218 \text{ km s}^{-1} < v < -140 \text{ km s}^{-1}$ which is in clear contradiction with the $[\text{Al}^+/\text{Al}^{++}]$ results. We believe that a significant portion of the SiIV absorption is due to gas which is physically separate from the low-ion and Al^{++} gas. As such, we consider the $[\text{Si}^+/\text{Si}^{3+}]$ values to be lower limits. To summarize, our results suggest the hydrogen fraction of the gas $\text{H}^0/\text{H} > 0.5$ is conservative lower limit. Therefore, it is highly likely that the gas in the $z = 2.46$ damped system is mainly neutral.

It is also likely that the neutrality of the gas is unaffected by the presence of *internal* sources of ionizing radiation such as O B stars. We checked this possibility by performing CLOUDY calculations with input from a black body with $T = 4 \times 10^4 \text{ K}$. The resulting $\text{Al}^+/\text{Al}^{++}$ and $\text{Si}^+/\text{Si}^{++}$ ratios are indistinguishable from the ratios predicted by the external radiation field considered above. The results are similar because the sharp drop in ionizing flux at the Lyman limit in the attenuated external spectrum (Madau 1992) mimics the exponential fall off of a black body. As a result the metal-line ratios indicate H is mainly neutral in the $z = 2.46$ absorber, for plausible sources of external and internal radiation.

7. RESULTS

This section presents the results from our abundance and kinematic analyses of the damped $\text{Ly}\alpha$ system at $z=2.462$. We discuss the evidence for dust in this system and remark on the nearly constant abundances relative to Zn for three of the velocity features in our system. Finally, we compare and contrast the kinematics of the damped $\text{Ly}\alpha$ system with several other systems, including another published HIRES damped $\text{Ly}\alpha$ system (Wolfe et al. 1994).

7.1. Abundances of the $z=2.462$ System

Table 12 lists the column density $\log[N(X)]$, and the logarithmic abundance of element X relative to hydrogen normalized to solar abundances, $[X/H] \equiv \log[N(X)/N(H)] - \log[N(X)/N(H)]_{\odot}$, for the damped Ly α system at $z=2.462$. The abundance is derived assuming $\log[N(H)] = 20.38 \pm 0.045$ (10% error) and standard solar abundances (Anders & Grevesse 1989). Our results indicate a relatively metal-rich system. If the three Zn⁺ features (discussed in §5.1) comprise 50% of the total Zn⁺ abundance (an analysis of these components in the other low-ions suggests $\approx 45\%$), we find $[Zn/H] = -0.262$. This is the most metal-rich of any damped Ly α system for which accurate abundances have been determined at redshift $z \geq 2.0$. Furthermore, it has a higher metallicity (assuming Zn predicts metallicity; see below) than all but one of the systems measured in the most extensive survey of metallicity in damped Ly α systems carried out so far (Pettini et al. 1994).

Figure 18 and Table 13 present the abundances of the low-ions relative to Zn (assuming cosmic abundances) in the three velocity features where we could reliably measure the Zn abundance. The error bars are not entirely accurate (they are derived with the apparent optical depth method), but do serve as valuable guides. The overall variation of the abundances relative to Zn is very small for the 3 features and all of the elements are depleted with respect to Zn. The values of $[X/Zn]$, however, do show a slight increase from the first to the third feature. We believe the most likely explanation lies in our measurements of the Zn abundance, particularly since features 1 and 2 are more likely to be blended with absorption from Cr II 2062 and because the trend is relatively systematic. Even given these minor differences, the relative abundances between Fe, Ni, Si, Cr and Zn are essentially constant over the 3 features (corresponding to nearly 200 km s⁻¹ in velocity space). Therefore, we see little evidence for gas-phase abundance variations throughout our system. This observation indicates damped Ly α systems are chemically well-mixed which further suggests they are detected at ages large compared to their internal dynamical time scales (i.e. the rotation period).

7.2. Dust Depletion

In this section we analyze variations of the gas-phase element abundances in damped Ly α systems with (a) velocity and (b) condensation temperature. Such variations have been observed in the ISM of the Galaxy and have been used to infer properties of the dust responsible for element depletion. We wish to see whether similar effects are present at high redshifts.

7.2.1. Abundance Variations

The absence of variations in $[X/Zn]$ with respect to velocity in the $z = 2.462$ system is contrary to the presence of such variations in the ISM. Spitzer & Fitzpatrick (1993) and Spitzer & Fitzpatrick (1995) recently used GHRs spectra to infer these variations for the sightlines to the Galactic stars HD 93521 and HD 149881. These sightlines are relevant because the measured $N(H^0)$ are similar to the value inferred for the damped system. Moreover, the depletion levels are similar, *provided one interprets negative values of $[X/Zn]$ in damped Ly α systems to result from grain depletion*. From Figure 18 and Table 13 we infer an upper limit of ≈ 0.3 dex for the variation of $[Si/Zn]$, $[Fe/Zn]$, $[Ni/Zn]$, or $[Cr/Zn]$ across the 3 velocity features in the $z = 2.46$ damped system, while the variation for $[Fe/Zn]$ in HD 93521 is ≈ 0.9 dex and for $[Cr/Zn]$ in HD 149881 is 0.6 dex (Spitzer and Fitzpatrick 1993, Spitzer and Fitzpatrick 1995). Fitzpatrick and Spitzer attribute the changes in $[X/Zn]$ to the increase in dust destruction for clouds with increasing random velocity with respect to galactic rotation speed.

Variations in $[X/Zn]$ could also be due to density variations along the line of sight. Studies of the ISM (Jenkins 1987) have shown correlations between the average Hydrogen volume density n_H and the degree of depletion D relative to cosmic abundances for a variety of elements, including Si, Cr, and Fe. Jenkins fitted the ISM data with the following depletion curve:

$$D = d_0 + m [\log n_H + 0.5] \quad (2)$$

where D is the logarithmic depletion relative to cosmic abundances (i.e., $[X/H]$), m is the slope, d_0 is the value of D at $\log n_H = -0.5$ and n_H is the Hydrogen volume density averaged over the line of sight to a given star. It is straightforward to show that the difference of two depletion values corresponding to two measurements ($\Delta D \equiv D_2 - D_1$) can be related to the ratio of the n_H values of each measurement:

$$\frac{(n_H)_2}{(n_H)_1} = 10^{|\frac{\Delta D}{m}|} \quad (3)$$

As stated above the variation of Si, Cr, and Fe relative to Zn over the 3 features is only ≈ 0.3 dex, where the largest variation is between the first and third features (the reddest and bluest). As suggested in §7.1 this variation is almost certainly systematic, most likely a result of blending with Cr II 2062. Therefore, the value can be considered an upper limit to the actual abundance variation over these 3 components. Table 14 lists the depletion variations, the ISM slopes cited in Jenkins (1987), the corresponding predicted n_H

variation, and 1σ errors for Fe, Si, and Cr. We note the Cr measurements place the tightest constraints on the predicted variation of n_H . Of course, the errors are rather large, but we can confidently predict that the variations of n_H are no larger than ≈ 1 dex provided this technique is applicable.

What suppresses variations of $[X/Zn]$ in the damped system? If dust is present, then the sightline through the damped system must encounter an ISM in which n_H varies by less than a factor of 10 along the line of sight. Moreover, the efficiency of grain destruction by shocks must be less efficient than in the ISM. Because the frequency of supernovae explosions account for the inhomogeneous nature of the ISM (McKee & Ostriker 1977) and because supernovae are the main contributor of shocks in the ISM, then a lower frequency of supernova explosions could account for the lack of variations in the damped system. However, in the ISM a sightline of a few kpc typically encounters 4 orders of magnitude variation in n_H (Kulkarni & Heiles 1987). A drastic reduction in the rate of supernova explosions would be required to reduce this to one order of magnitude. But models for the evolution of disk galaxies suggest that supernova input in the past was stronger not weaker than in the present (Bruzual 1992). Other, nucleosynthetic considerations suggest that supernovae rates in the past were as least as frequent as they are at present (Truran 1995). Therefore, while we cannot rule out this explanation altogether, it seems implausible.

Therefore, the null detection of variations in $[X/Zn]$ requires a weaker coupling of the depletion rate to the gas density, and a lower grain destruction rate by interstellar shocks than in the ISM. As a result, dust in the damped system is either absent or has significantly different properties from dust in the ISM.

7.2.2. Condensation Temperature

Figure 19 plots the gas phase abundances versus condensation temperature, T_C , for the observed low-ions from the damped Ly α system (solid dots) and from the line-of-sight toward the Galactic star ζ Oph (Cardelli 1994; open squares³). The idea is to determine whether the anti-correlation between $[X/H]$ and T_C observed in the ISM (Jenkins 1987) is also present in high- z damped Ly α systems. Because T_C is the temperature at which half the gas phase atoms in a stellar atmosphere condense to solid form, the ISM anti-correlation is taken as evidence for dust formation in stellar atmospheres (Field 1974). Comparison between the ISM and damped diagrams shows some similarities. Specifically, the relative rankings of $[Cr/H]$, $[Si/H]$, $[Fe/H]$, and $[Ni/H]$ are about the same. However, the absolute

³The error bars for the ISM data are on the order of the size of the squares or smaller.

values are significantly higher in the damped system. In addition $[\text{Zn}/\text{H}]$ in the ISM greatly exceeds all the other $[\text{X}/\text{H}]$, but in the damped system $[\text{Zn}/\text{H}]$ does not greatly exceed $[\text{Cr}/\text{H}]$, $[\text{Fe}/\text{H}]$, and $[\text{Ni}/\text{H}]$, and may in fact be comparable to $[\text{Si}/\text{H}]$. The differences between the ISM and damped $[\text{X}/\text{H}]$ may indicate the presence of gas in which the metallicity (inferred from undepleted $[\text{Zn}/\text{H}]$) is > -0.5 and has a lower dust-to-gas ratio to account for the smaller difference between $[\text{Zn}/\text{H}]$ and $[\text{X}/\text{H}]$ (cf. Pettini et al. 1994).

On the other hand, Lu et al. (1995, 1996a, 1996b) interpret these patterns in terms of nucleosynthetic yields from type II supernovae. They point out that the damped Ly α abundance patterns of N/O, Si/Fe, Cr/Fe, and Mn/Fe are consistent with the abundance patterns observed for population II halo stars which have been primarily enriched by type II supernovae (Wheeler et al. 1989). They also stress that Mn/Fe for damped Ly α systems and halo stars disagrees with Mn/Fe inferred for the ISM, which is influenced by grain depletion. The only difficulties with the Lu et al. hypothesis stem from Zn/Fe. The quantity $[\text{Zn}/\text{Fe}] > 0$ in damped Ly α systems, while $[\text{Zn}/\text{Fe}] \approx 0$ for stars with $-3 < [\text{Fe}/\text{H}] < 0$ (Snedden et al. 1991).

Theorists working on chemical evolution have long been puzzled as to why $[\text{Zn}/\text{Fe}]$ is independent of $[\text{Fe}/\text{H}]$. The closed box model by Malaney and Chaboyer (1996) predicts $[\text{Zn}/\text{Fe}]$ to increase with $[\text{Fe}/\text{H}]$ owing to the metallicity-dependent yield computed for type II supernovae explosions. These authors suggest that the constant $[\text{Zn}/\text{Fe}]$ could be peculiar to the chemical evolution of the Galaxy, due to non-LTE effects in stellar atmospheres, or errors in the calculated yields. In addition, while the Malaney-Chaboyer model predicts $[\text{Zn}/\text{Fe}] < 0$, Hoffman et al. (1996) suggest neutrino driven winds in type II supernovae might result in $[\text{Zn}/\text{Fe}] > 0$. This effect may help explain the overabundance of Zn relative to Fe in damped Ly α systems. Therefore, while some questions remain to be addressed, nucleosynthetic yields and grain depletion are equally plausible explanations for the abundance patterns observed in damped Ly α systems.

These competing explanations lead to at least two different ways for interpreting the metallicity of damped Ly α systems. First, if the Lu et al. interpretation is correct and Zn is somehow overproduced with respect to Fe, then the metallicity of damped Ly α systems is significantly lower (≈ 0.7 dex) than estimated from the Zn abundances. In terms of the system analyzed in this paper, the metallicity would be -0.83 dex which would still be the highest metallicity observed in a damped Ly α system with $z > 2.0$. On the other hand, if we accept depletion, the metallicity of these systems is at least as high as the Zn abundance, and the Malaney-Chaboyer results indicate it could be even higher (possibly requiring an even greater level of depletion).

7.3. Kinematics of the Damped Ly α System ($z=2.462$)

In this subsection we discuss the kinematics of the damped Ly α system at $z=2.462$. We stress again the observed differences between the high and low-ion profiles and intercompare the velocity profiles of the $z=2.462$ system and several other damped systems.

7.3.1. Comparison of the Low and High Ion Profiles

Although all of the transitions from the $z = 2.462$ system span approximately the same velocity interval ($\approx 200 \text{ km s}^{-1}$), there are marked differences between the low and high-ion line profiles. Similar to the damped Ly α system toward PHL 957 discussed by Wolfe et al. (1994), the velocity profiles of all of the low-ions are visibly asymmetric with the component at the red edge being the strongest of the profile. In this case, the strongest component is at the red edge, where in PHL957 the strongest component is at the blue edge. Figure 20 and Table 15 give the column density by percent of total in 5 binned intervals in velocity space corresponding to visible features in the line profiles. This serves as quantitative evidence of the asymmetry in the low-ions and highlights the inherent differences between the low and high-ion profiles. The overall profile of the high-ions has nearly the opposite shape of the low-ion profiles with the strongest feature on the blue edge. In addition, the profile of the high-ions is smoother with less structure than the low ions.

We contend these differences, particularly those evident in the Si II and Si IV profiles, indicate the absorption associated with the high-ions does not originate in the same region as that associated with the low-ions. The most compelling evidence for this hypothesis lies in the extreme difficulty encountered in obtaining an accurate fit to the Si IV profile by altering the column densities of the calculated Si II components while holding the redshift and b values constant. Both the smoothness and the overall shape of the Si IV profile require significantly different b values and argue against the inclusion of so many thin, resolved components.

7.3.2. The $z=2.457$ subsystem

The neighboring system at $z=2.457$ was unidentified in the lower resolution data. It has similar line profile structure as the $z=2.462$ system with a large velocity interval, smoother high-ion profiles and low-ion profiles with more velocity structure. It does not, however, exhibit the edge leading asymmetry apparent in the $z=2.462$ system. In fact, the low-ions appear relatively symmetric about $v = 70 \text{ km s}^{-1}$. We contend these differences in

the kinematic characteristics result from the fact that the $z=2.457$ system is not a damped Ly α system but most likely an ionized Lyman limit system in which the gas kinematics are not determined by rotation.

7.3.3. Comparison with PHL 957

Contrasting the damped Ly α metal transitions with those toward PHL 957 at $z = 2.309$, we note several important differences. First, the velocity interval of the Q0201+365 damped system is significantly larger (200 km s^{-1} vs. 50 km s^{-1}). Secondly, the low-ions of the Q0201+365 system exhibit more velocity structure, an effect which is not due to differences in resolution. Finally, the asymmetric shape is not as prevalent in our damped system possibly because of its larger velocity interval. That is, the gas is more evenly distributed in Q0201+365 than in the PHL957 absorber. In terms of the thick rotating disk model, these differences may be explained by differences in the inclination angle of the line-of-sight with respect to the disk.

7.3.4. Comparison with System at $z = 2.325$

A comparison of the damped Ly α kinematics with the absorption system at $z = 2.325$ toward Q0201+365 further stresses the damped Ly α characteristics. The $z = 2.325$ system (a possible Lyman limit system) also spans $\approx 200 \text{ km s}^{-1}$ in velocity space, but does not possess the same edge-leading asymmetric profile observed in the damped systems. Furthermore, the high-ion profiles at $z=2.325$ trace the low-ion profiles more closely than in the damped Ly α systems. For instance, Al III was successfully tied to the low-ion VPFIT solution. These characteristics are all consistent with an explanation depicting the $z=2.325$ system as a multi-cloud system in which the velocities are random rather than systematic as in the case of rotation. Moreover the gas is more evenly distributed. In short, the $z = 2.325$ system more closely resembles the $z=2.457$ system which is also a likely Lyman limit system. Perhaps we are observing kinematic characteristics which differentiate damped Ly α from Lyman limit systems. However, the statistics of small numbers makes this observation a speculation rather than a conclusion.

8. CONCLUSIONS

This paper presented HIRES spectra obtained with the Keck 10m telescope of absorbing gas toward toward Q0201+365. We identified over 80% of the absorption features and have analyzed several of the more interesting metal-line systems. We have focused on the damped Ly α system at $z=2.462$ as part of an ongoing program to investigate the chemical content and kinematics of damped systems within the redshift interval $z \approx 2 - 4$. We summarize our results as follows.

(1) Based on the analysis of ionization simulations, we predict the damped Ly α system to be significantly neutral. Although it is possible the system is partially ionized, our analysis predicts the metals are all essentially in the singly ionized state, and that the total hydrogen column density is well within a factor of two of the adopted value from the $N(\text{H}^0)$ measurement.

(2) A hidden component analysis of the Ni II 1741, 1751 transitions did not reveal any significant hidden saturated components. We expect this to hold true for the other low-ion transitions.

(3) With the VPFIT least squares line profile fitting package we have measured ionic column densities for the damped Ly α system at $z=2.462$ (as well as several other systems). We performed similar measurements with the apparent optical depth method and found the two results to be in agreement, further eliminating the possibility of hidden line saturation.

(4) We measured the following abundances of Si, Fe, Cr, and Ni for the damped Ly α system: $[\text{Si}/\text{H}] = -0.376 \pm 0.052$, $[\text{Fe}/\text{H}] = -0.830 \pm 0.051$, $[\text{Cr}/\text{H}] = -0.902 \pm 0.064$, and $[\text{Ni}/\text{H}] = -1.002 \pm 0.054$. We placed limiting values on the abundances of the s-process elements Pb (3σ detection) and Ge (upper limit), $[\text{Pb}/\text{H}] = 2.233 \pm 0.121$ and $[\text{Ge}/\text{H}] < 0.664$, and a lower limit value on the abundance of Zn, $[\text{Zn}/\text{H}] > -0.562$. Based on the VPFIT solution of the low-ions, we expect the metallicity is $[Z/\text{H}] \approx -0.262$. This damped Ly α system has the highest metallicity measured to date at $z \geq 2.0$.

(5) Comparing individual features of the damped Ly α system, we find the relative abundance between Si, Fe, Cr, Ni and Zn remains nearly constant throughout our system (Figure 13). This suggests a well mixed system with an age large compared to the internal dynamical time scale at the epoch of detection.

(6) We have used the relatively minor variations observed in the Si, Cr, and Fe abundances relative to Zn to place limits on the expected variation in the Hydrogen volume density throughout the damped Ly α system, having assumed the presence of dust grains and the Jenkins relation (Jenkins 1987). Our measurements of $[\text{Cr}/\text{Zn}]$ place a maximum

variation of n_H at ≈ 1 dex. The lack of n_H (and $[X/Zn]$) variations could be evidence of weaker supernova input in the past, but we believe they are more likely due to the absence of grains with the properties of dust found in the ISM.

(7) Plotting the measured abundances versus condensation temperature (Figure 19), we do find evidence for a depletion pattern, but the overall depletion level of Si, Fe, Cr and Ni with respect to Zn is indicative of a relatively dust free ISM cloud. Although gas with a lower dust-to-gas ratio than evident in the ISM can account for the pattern, one can also explain the pattern in terms of nucleosynthetic yields from type II supernovae (Lu, Sargent, & Barlow 1995). Both explanations are problematic and are under continued debate. Determining the proper explanation is particularly important as they predict different metallicities for damped Ly α systems, which will significantly affect the investigation of galactic chemical evolution.

(8) The low-ion profiles of the damped system exhibit an edge leading asymmetry as predicted by a simple model of rotation. The shape is similar to the other damped system observed with HIRES (PHL 957; Wolfe et al. 1994), though the velocity interval is significantly greater.

The authors would like to thank Bob Carswell for providing the line-profile fitting package VPFIT as well as Tom Barlow for his excellent HIRES data reduction software. We would also like to thank Vincent Virgilio for his help in developing the neutral hydrogen model and Piero Madau for providing the ionizing spectrum. Finally, we would like to thank Ed Jenkins and Edward Fitzpatrick for helpful discussions. AMW and JXP were partially supported by NASA grant NAGW-2119 and NSF grant AST 86-9420443.

UT Date	Exposure Time (s)	Wavelength Coverage (\AA)	Resolution (km s^{-1})
1994 Sep 15	9600	4720 - 7130	7.2 - 8.0
1994 Sep 30	11950	4790 - 7180	7.0 - 8.0
1994 Oct 1	13030	4790 - 7180	7.2 - 8.1

Table 1: JOURNAL OF OBSERVATIONS

Table 2. ABSORPTION LINE LIST

Order	λ (\AA)	W (\AA)	σ_W	ID	z_{abs}
75	4724.79	0.1891	0.0101		
	4727.73	0.1681	0.0089		
	4730.96	0.0456	0.0049		
	4737.23	0.2245	0.0081		
	4739.54	0.3687	0.0076		
	4742.94	0.3541	0.0132	NiII(1370)	2.462
	4750.76	0.1077	0.0062		
	4753.96	1.8529	0.0125	FeII(1608)	1.956
	4758.58	1.6854	0.0073		
	4761.95	0.0246	0.0038	FeII(1611)	1.956
	4763.30	0.0170	0.0031		
	4768.05	0.0344	0.0040	SiIV(1393)	2.421
	4770.63	0.2802	0.0067	SiIV(1393)	2.423
	4772.64	B ^a		SiIV(1393)	2.424
	4773.34	B ^a			
	4783.89	0.9927	0.0099		
74	4784.71	0.2125	0.0053		
	4798.95	0.0257	0.0029	SiIV(1402)	2.421
	4802.23	0.1792	0.0082	SiIV(1402)	2.423
	4808.08	0.0957	0.0046		
	4809.61	0.0474	0.0029		
	4817.94	1.5530	0.0104	SiIV(1393)	2.457
	4824.06	1.9596	0.0105	SiIV(1393)	2.462
	4842.24	1.6780	0.0067	MgII(2796)	0.732
	4847.31	B ^a		MgII(2796)	0.733
	4849.94	B ^a		SiIV(1402)	2.457
	4852.51	0.0287	0.0052		
	73	4850.48	0.3522	0.0067	SiIV(1402)
4855		B ^a		MgII(2803)	0.731
4855		B ^a		SiIV(1402)	2.462
4859.84		0.2065	0.0061	MgII(2803)	0.733
4863.60		0.0227	0.0026		
4876.08		0.0190	0.0028		
4895.98		0.0982	0.0087	Cl(1656)	1.955
72		4924.10	0.1703	0.0073	ClI(1334)
	4938	B ^a		AlI(1671)	1.955
	4940	B ^a		MgI(2852)	0.732
	4951.84	0.2428	0.0112	SiIV(1393)	2.553
	4984.16	0.2462	0.0152	SiIV(1402)	2.553
	71	5005.84	1.3215	0.0112	ClV(1548)
5014.00		0.8942	0.0101	ClV(1550)	2.233
70	5076.49	1.3223	0.0153	SiII(1526)	2.325
69	5139.61	0.3223	0.0059	ClV(1548)	2.320
	5142.70	0.7369	0.0094	SiIV(1393)	2.690
	5148	B ^a		ClV(1548)	2.325
	5148.15	B ^a		ClV(1550)	2.319
	5156.16	2.0353	0.0133	ClV(1550)	2.325
	5172.86	S ^b		Sky Emiss	
	5175.62	0.8012	0.0136	SiIV(1402)	2.690
	5177.77	0.0241	0.0035		
	5189.73	0.0407	0.0054	Cl(1560)	2.325
	5200.18	0.0301	0.0054	Sky??	
	5201.43	0.0609	0.0057	ClV(1548)	2.360

Table 2—Continued

Order	λ (Å)	W (Å)	σ_W	ID	z_{abs}
68	5210.07	0.0330	0.0047	CIV(1550)	2.360
	5234.86	0.0337	0.0049	Sky Abs	
	5270.54	0.1121	0.0076		
	5272.51	0.2489	0.0128		
	5275.32	0.1389	0.0077		
	5278.45	1.5553	0.0177	SiII(1526)	2.457
67	5285.95	3.3202	0.0121	SiII(1526)	2.462
	5298.86	2.4749	0.0171	CIV(1548)	2.423
	5307.77	1.7411	0.0164	CIV(1550)	2.423
	5326.05	0.3089	0.0069	SiIV(1393)	2.821
	5342.40	0.2902	0.0131	SiII(1808)	1.955
	5347.39	0.2201	0.0148	FeII(1608)	2.325
	5352.75	3.2158	0.0166	CIV(1548)	2.457
	5357.45	2.3480	0.0169	CIV(1548)	2.462
66	5367.53	2.1787	0.0194	CIV(1550)	2.462
	5373.05	0.2364	0.0091	CIV(1550)?	2.465
	5383.04	0.3361	0.0130	CIV(1548)	2.477
	5391.61	0.1891	0.0124	CIV(1550)	2.477
	5419.45	0.4062	0.0097	CIV(1548)	2.500
	5425.90	S ^b		Sky Abs	
	5428.50	0.2452	0.0112	CIV(1550)	2.500
65	5458.78	0.0286	0.0039		
	5481.60	1.3494	0.0128	AlIII(1854)	1.955
	5500.98	1.5163	0.0100	CIV(1548)	2.553
	5505.02	0.7522	0.0135	AlIII(1862)	1.955
	5510.20	0.9414	0.0119	CIV(1550)	2.553
	5512.77	0.0255	0.0042		
64	5555.32	1.3290	0.0144	AlII(1671)	2.325
	5560.52	0.2871	0.0130	FeII(1608)	2.457
	5568.31	2.6714	0.0117	FeII(1608)	2.462
	5579.22	B ^a		FeII(1611)	2.462
	5607.50	0.0793	0.0079		
63	5622.07	0.0397	0.0062		
62	5713.13	1.0943	0.0136	CIV(1548)	2.690
	5722.31	0.6010	0.0125	CIV(1550)	2.690
	5776.46	2.1480	0.0137	AlII(1671)	2.457
	5783.40	5.0321	0.0164	AlII(1671)	2.462
61	5804.51	0.5622	0.0091	FeII(2344)	1.476
	5845.15	0.0226	0.0044		
	5872.81	0.0190	0.0037	FeII(2374)	1.473
	5874.03	0.1010	0.0072	FeII(2374)	1.474
	5879.60	0.2519	0.0072	FeII(2374)	1.476
60	5901.21	0.4404	0.0099	FeII(2382)	1.476
	5916.32	B ^a		CIV(1548)?	2.821
	5919	B ^a		NiII(1709)	2.462
	6076.31	0.0191	0.0033	CrII(2056)	1.955
59	6010.37	0.0947	0.0127	SiII(1808)	2.325
	6028.97	0.3928	0.0113	NiII(1741)	2.462
	6043.72	S ^b		Ink Blot	
	6064.91	0.2400	0.0110	NiII(1751)	2.462

Table 2—Continued

Order	λ (Å)	W (Å)	σ_W	ID	z_{abs}
58	6166.72	0.6211	0.0140	AlIII(1854)	2.325
57	6259.01	0.6740	0.0140	SiII(1808)	2.462
	6280 -	S ^b		Sky Abs	
56	6327.85	0.3591	0.0090	FeII(2344)	1.699
	6331.86	S ^b		Sky Abs	
	6366	S ^b		Sky Abs	
	6380.61	S ^b		Sky Abs	
	6398.86	0.2889	0.0095	FeII(2586)	1.473
	6400.33	0.0246	0.0040	FeII(2586)	1.474
	6403.12	0.0902	0.0061	FeII(2586)	1.475
	6404.76	0.5519	0.0089	FeII(2586)	1.476
	6411.14	0.2570	0.0113	FeII(2374)	1.699
55	6438.10	0.9346	0.0102	FeII(2600)	1.476
	6440.63	0.2097	0.0109	AlIII(1863)	2.457
	6448.40	0.9757	0.0148	AlIII(1863)	2.462
	6470 -	S ^b		Sky Abs	
54					
53					
52	6813.84	0.0381	0.0053		
	6869 -	S ^b		Band Abs	
51	6942.03	0.9711	0.0084	MgII(2803)	1.476
	6944.50	S ^b		Sky Abs	
	6946.10	S ^b		Sky Abs	
	6958.54	S ^b		Sky Abs	
	6963.62	S ^b		Sky Abs	
	6982.78	0.2482	0.0105	FeII(2586)	1.699
	6987.39	S ^b		Sky Abs	
	6988.89	S ^b		Sky Abs	
	6991.29	S ^b		Sky Abs	
	6995.81	S ^b		Sky Abs	
	7001.26	S ^b		Sky Abs	
	7007.03	S ^b		Sky Abs	
	7016	B ^a		FeII(2374)	1.955
	7018.78	B ^a		FeII(2600)	1.699
	7039.67	1.6433	0.0080	FeII(2382)	1.955
50	7118.18	0.2471	0.0159	CrII(2056)	2.462
	7140.5	B ^a		CrII(2062)	2.462
	7140.5	B ^a		ZnII(2062)	2.462
	7144 -	S ^b		H ₂ O Abs	

^a Line blending

^b Night-sky absorption or emission features

Table 3. METAL TRANSITIONS

Transition	$\lambda_{\text{rest}} (\text{\AA})$	f
NiII 1370	1370.132	0.1309
SiIV 1393	1393.755	0.528
SnII 1400	1400.400	0.71
SiIV 1402	1402.770	0.262
GaII 1414	1414.402	1.8
SiII 1526	1526.707	0.2303
CIV 1548	1548.195	0.1908
CIV 1550	1550.770	0.09522
GeII 1602	1602.4863	0.135
FeII 1608	1608.4449	0.05545
AlII 1670	1670.7874	1.88
PbII 1682	1682.15	0.156
NiII 1741	1741.549	0.1035
NiII 1751	1751.910	0.0638
SiII 1808	1808.0126	0.00218
AlIII 1854	1854.716	0.539
AlIII 1862	1862.790	0.268
ZnII 2026	2026.136	0.515
CrII 2056	2056.254	0.1403
CrII 2062	2062.234	0.1049
ZnII 2062	2062.664	0.2529
FeII 2344	2344.214	0.1097
FeII 2374	2374.4612	0.02818
FeII 2382	2382.765	0.3006
FeII 2600	2600.1729	0.2239
MgII 2796	2796.352	0.6123
MgII 2803	2803.531	0.3054

Table 4a. FIT FOR $z=2.462$ – LOW IONS

Comp	z	σ_z $\times 10^{-5}$	b (km s^{-1})	σ_b (km s^{-1})	ION	$\log N$ (cm^{-2})	$\sigma_{\log N}$ (cm^{-2})
1	2.460470	2.0	4.59	2.19	Fe ⁺	13.11	0.15
2	2.460598	0.3	4.44	0.47	Fe ⁺	14.11	0.05
					Si ⁺	14.41	0.04
					Ni ⁺	12.56	0.04
					Cr ⁺	12.02	0.10
3	2.460807	0.5	5.91	1.01	Fe ⁺	13.99	0.13
					Si ⁺	14.36	0.16
					Ni ⁺	12.30	0.32
					Cr ⁺	12.18	0.12
4	2.460944	5.9	12.47	4.97	Fe ⁺	13.80	0.24
					Si ⁺	14.21	0.25
					Ni ⁺	12.54	0.22
					Cr ⁺	11.61	0.55
5	2.461347	1.4	13.94	1.17	Fe ⁺	13.99	0.04
					Si ⁺	14.52	0.06
					Ni ⁺	12.64	0.07
					Cr ⁺	12.28	0.12
6	2.461426	0.5	3.00	1.22	Fe ⁺	13.74	0.10
					Si ⁺	13.94	0.17
					Ni ⁺	12.00	0.19
					Cr ⁺	11.69	0.31
7	2.461735	0.4	8.56	0.63	Fe ⁺	14.20	0.02
					Si ⁺	14.76	0.03
					Ni ⁺	12.85	0.03
					Cr ⁺	12.23	0.08
8	2.461905	0.4	3.24	0.89	Fe ⁺	13.92	0.08
					Si ⁺	14.33	0.07
					Ni ⁺	12.45	0.07
					Cr ⁺	11.96	0.13
9	2.462091	1.4	8.23	2.59	Fe ⁺	13.68	0.11
					Si ⁺	14.19	0.14
					Ni ⁺	12.30	0.12
					Cr ⁺	11.06	1.15
10	2.462266	1.5	6.22	2.42	Fe ⁺	13.51	0.19
					Si ⁺	14.13	0.19
					Ni ⁺	11.94	0.30
					Cr ⁺	11.02	1.22
11	2.462494	2.2	11.31	2.43	Fe ⁺	13.99	0.10
					Si ⁺	14.59	0.11
					Ni ⁺	12.59	0.11
					Cr ⁺	12.27	0.10
12	2.462594	0.6	3.00	1.49	Fe ⁺	13.88	0.18
					Si ⁺	14.17	0.17
					Ni ⁺	12.18	0.18
13	2.462818	0.6	14.58	0.56	Fe ⁺	14.43	0.02
					Si ⁺	14.92	0.02
					Ni ⁺	13.00	0.02
					Cr ⁺	12.57	0.05

Comp	z	σ_z ($\times 10^{-5}$)	b (km s^{-1})	σ_b (km s^{-1})	Ion	$\log N$ (cm^{-2})	$\sigma_{\log N}$ (cm^{-2})
1	2.459346	2.5	18.33	3.03	Si ⁺³	11.72	0.53
					C ⁺³	13.47	0.07
2	2.459713	4.4	43.14	8.77	Si ⁺³	12.81	0.12
					C ⁺³	13.95	0.04
3	2.460433	1.0	9.43	0.99	Si ⁺³	12.77	0.07
					C ⁺³	13.45	0.10
4	2.460753	1.2	16.65	1.50	Si ⁺³	13.45	0.04
					C ⁺³	14.19	0.13
5	2.461035	0.8	11.63	0.64	Si ⁺³	13.54	0.04
					C ⁺³	13.10	0.24
6	2.461647	22.3	82.54	22.64	Si ⁺³	13.36	0.14
					C ⁺³	12.85	0.38
7	2.461863	0.9	15.01	1.61	Si ⁺³	12.81	0.08
					C ⁺³	13.41	0.48
8	2.462229	3.5	11.01	5.97	Si ⁺³	11.67	0.52
9	2.462762	9.1	38.26	11.23	Si ⁺³	12.81	0.31
					C ⁺³	13.35	0.11
10	2.462908	2.1	5.38	5.93	Si ⁺³	11.59	0.34
					C ⁺³	13.63	0.12

Table 4b: FIT FOR $z=2.462$ – HIGH IONS

Table 5a. FIT FOR $z=2.457$ – LOW IONS

Comp	z	σ_z $\times 10^{-5}$	b (km s^{-1})	σ_b (km s^{-1})	ION	$\log N$ (cm^{-2})	$\sigma_{\log N}$ (cm^{-2})
1	2.456041	0.5	3.95	0.80	Si ⁺	12.53	0.06
					Fe ⁺	12.34	0.20
					Al ⁺	11.81	0.04
2	2.456295	0.3	9.58	0.49	Si ⁺	13.40	0.02
					Fe ⁺	13.19	0.04
					Al ⁺	12.60	0.02
3	2.456540	1.5	5.44	2.57	Si ⁺	12.54	0.15
					Fe ⁺	12.30	0.29
					Al ⁺	11.78	0.12
4	2.456679	0.6	3.30	1.30	Si ⁺	13.03	0.05
					Fe ⁺	12.78	0.12
					Al ⁺	12.19	0.06
5	2.456844	1.6	8.95	2.88	Si ⁺	12.98	0.18
					Fe ⁺	12.95	0.14
					Al ⁺	12.26	0.16
6	2.457079	1.5	12.83	1.78	Si ⁺	13.41	0.06
					Fe ⁺	13.04	0.10
					Al ⁺	12.65	0.06
7	2.457336	0.6	3.00	1.15	Si ⁺	13.21	0.11
					Fe ⁺	12.78	0.09
					Al ⁺	12.28	0.11
8	2.457460	0.6	3.00	1.22	Si ⁺	13.16	0.10
					Fe ⁺	12.63	0.12
					Al ⁺	12.22	0.09
9	2.457689	6.4	25.16	7.00	Si ⁺	13.04	0.13
					Al ⁺	12.37	0.11
10	2.457858	0.3	6.37	0.57	Si ⁺	13.35	0.04
					Fe ⁺	13.11	0.05
					Al ⁺	12.42	0.05
11	2.458100	1.1	4.65	2.29	Si ⁺	12.40	0.15
					Fe ⁺	12.17	0.30
					Al ⁺	11.42	0.25
12	2.458406	0.8	14.96	1.20	Si ⁺	12.80	0.05
					Al ⁺	12.09	0.03

Comp	z	σ_z ($\times 10^{-5}$)	b (km s^{-1})	σ_b (km s^{-1})	Ion	$\log N$ (cm^{-2})	$\sigma_{\log N}$ (cm^{-2})
1	2.456343	0.7	24.36	0.78	Si ⁺³	12.98	0.02
					C ⁺³	13.86	0.02
2	2.457273	0.5	34.58	0.70	Si ⁺³	13.65	0.01
					C ⁺³	14.54	0.02
3	2.457873	0.4	8.77	0.61	Si ⁺³	12.98	0.02
					C ⁺³	13.75	0.05
4	2.458106	0.9	7.53	1.17	Si ⁺³	12.45	0.06
					C ⁺³	13.32	0.07
5	2.458454	1.5	30.67	1.98	Si ⁺³	12.67	0.04
					C ⁺³	13.77	0.03

Table 5b: FIT FOR $z=2.457$ – HIGH IONS

Table 6a. FIT FOR $z=2.325$ – LOW IONS

Comp	z	σ_z $\times 10^{-5}$	b (km s^{-1})	σ_b (km s^{-1})	ION	$\log N$ (cm^{-2})	$\sigma_{\log N}$ (cm^{-2})
1	2.323701	0.6	6.87	0.99	Al ⁺	11.52	0.06
					Al ⁺²	11.97	0.05
					Fe ⁺	11.87	0.78
					Si ⁺	12.73	0.04
2	2.323896	0.3	3.39	0.57	Al ⁺	13.00	0.25
					Al ⁺²	12.59	0.03
					Fe ⁺	13.32	0.04
					Si ⁺	13.92	0.24
3	2.324033	0.3	3.37	0.69	Al ⁺	12.83	0.23
					Al ⁺²	12.48	0.03
					Fe ⁺	13.30	0.04
					Si ⁺	13.81	0.26
4	2.324173	1.0	3.41	1.86	Al ⁺²	11.81	0.07
					Al ⁺	11.63	0.11
5	2.324195	2.8	9.92	3.16	Si ⁺	12.22	0.17
					Al ⁺	12.28	0.02
6	2.324663	0.2	6.24	0.26	Al ⁺²	12.02	0.04
					Fe ⁺	12.71	0.13
					Si ⁺	13.21	0.02
					Al ⁺	11.11	0.12
7	2.324884	1.2	2.80	2.97	Si ⁺	11.98	0.15
					Al ⁺	11.97	0.05
					Al ⁺²	11.92	0.06
8	2.325078	0.7	3.12	0.88	Fe ⁺	12.47	0.22
					Si ⁺	13.06	0.06
					Al ⁺	13.03	0.70
					Al ⁺²	11.99	0.06
9	2.325180	0.4	2.27	0.78	Fe ⁺	13.36	0.07
					Si ⁺	14.30	0.76
					Al ⁺	11.45	0.06
					Al ⁺²	11.65	0.09
10	2.325560	0.6	5.56	1.02	Fe ⁺	12.01	0.56
					Si ⁺	12.47	0.06
					Al ⁺	11.20	0.10
					Al ⁺²	12.16	0.03
11	2.325796	1.5	4.88	2.55	Al ⁺	12.11	0.04
					Fe ⁺	12.46	0.20
12	2.326045	0.3	4.68	0.39	Si ⁺	13.34	0.03
					Al ⁺	12.08	0.03
					Al ⁺²	12.09	0.04
					Fe ⁺	12.75	0.12
13	2.326198	0.5	6.88	0.54	Si ⁺	13.21	0.03

Comp	z	σ_z ($\times 10^{-5}$)	b (km s^{-1})	σ_b (km s^{-1})	Ion	$\log N$ (cm^{-2})	$\sigma_{\log N}$ (cm^{-2})
1	2.319744	0.2	9.11	0.29	C ⁺³	13.64	0.01
2	2.323508	4.4	15.48	3.55	C ⁺³	13.13	0.13
3	2.323736	1.2	9.13	1.83	C ⁺³	13.47	0.16
4	2.324048	1.4	24.68	2.38	C ⁺³	14.25	0.04
5	2.324569	2.4	15.07	3.74	C ⁺³	13.56	0.13
6	2.324825	1.9	11.15	2.60	C ⁺³	13.41	0.18
7	2.325100	3.8	16.40	4.30	C ⁺³	13.25	0.12
8	2.325624	0.7	18.12	1.23	C ⁺³	13.47	0.02
9	2.326123	0.2	14.21	0.25	C ⁺³	14.23	0.01

Table 6b: FIT FOR $z=2.325$ – HIGH IONS

Comp	z	σ_z ($\times 10^{-5}$)	b (km s^{-1})	σ_b (km s^{-1})	Ion	$\log N$ (cm^{-2})	$\sigma_{\log N}$ (cm^{-2})
1	1.475760	1.5	1.21	5.88	Fe ⁺	12.24	0.18
2	1.475858	0.7	4.27	1.87	Fe ⁺	12.71	0.07
3	1.476039	0.4	3.59	0.52	Fe ⁺	13.65	0.03
4	1.476115	0.8	2.44	1.37	Fe ⁺	13.22	0.06
5	1.476182	0.9	2.05	1.86	Fe ⁺	12.92	0.08
6	1.476301	0.1	2.70	0.22	Fe ⁺	13.64	0.04

Table 7: FIT FOR $z=1.476$

Transition	Apparent	VPFIT	Adopted
Si IV 1393	14.039 ± 0.006	14.050 ± 0.038	14.045 ± 0.038
C IV 1550	14.617 ± 0.005	14.615 ± 0.062	14.616 ± 0.062
C I 1560	13.228 ± 0.059		13.228 ± 0.059
Fe II 1608	15.033 ± 0.004	15.086 ± 0.024	15.060 ± 0.024
Al II 1671			
Ni II 1709	13.785 ± 0.020		13.785 ± 0.020
Ni II 1741	13.638 ± 0.013	13.631 ± 0.030	13.628 ± 0.030
Ni II 1751	13.610 ± 0.020		
Si II 1808	15.561 ± 0.010	15.546 ± 0.026	15.554 ± 0.026
Al III 1862	13.606 ± 0.008		13.606 ± 0.008
Cr II 2056	13.158 ± 0.030	13.138 ± 0.040	13.148 ± 0.040
Cr II 2062	13.401 ± 0.025		13.401 ± 0.025
Zn II 2062	12.468 ± 0.046		12.468 ± 0.046
Pb II 1682	12.66 ± 0.114		12.66 ± 0.114
Ge II 1602	< 12.65		< 12.65

Table 8: IONIC COLUMN DENSITIES FOR $z = 2.462$

Note. — Values reported in logarithmic space have deceptively small errors. For instance, the value for $N(\text{Pb})$ is not a 5σ detection and that for $N(\text{Ge})$ is not even a 1σ detection.

Transition	Apparent	VPFIT	Adopted
Si IV 1393	13.839 ± 0.003	13.85 ± 0.01	13.85 ± 0.01
Si IV 1403	13.851 ± 0.007		13.85 ± 0.01
C IV 1550	14.686 ± 0.041	14.74 ± 0.01	14.737 ± 0.010
Si II 1526	14.129 ± 0.006	14.18 ± 0.02	14.18 ± 0.02
Fe II 1608	13.839 ± 0.022	13.85 ± 0.03	13.843 ± 0.018
Al II 1671	13.321 ± 0.004	13.36 ± 0.02	13.36 ± 0.02
Al III 1862	12.920 ± 0.028		12.920 ± 0.028

Table 9: IONIC COLUMN DENSITIES FOR $z = 2.457$

Component	$\log_{10} N(\text{HI})$	z_{abs}	b (km s ⁻¹)
1	18.38	2.460470	4.59
2	19.38	2.460598	4.44
3	19.26	2.460807	5.91
4	19.07	2.460944	12.47
5	19.26	2.461347	13.94
6	19.01	2.461426	3.00
7	19.47	2.461735	8.56
8	19.18	2.461905	3.24
9	18.95	2.462091	8.23
10	18.78	2.462266	6.22
11	19.26	2.462494	11.31
12	19.15	2.462594	3.00
13	19.70	2.462818	14.58
14	17.61	2.456041	3.95
15	18.46	2.456295	9.58
16	17.57	2.456540	5.44
17	18.05	2.456679	3.30
18	18.22	2.456844	8.95
19	18.31	2.457079	12.83
20	18.05	2.457336	3.00
21	17.90	2.457460	3.00
22	18.38	2.457858	6.37
23	17.44	2.458100	4.65

Table 10: HI COMPONENTS IN Ly α PROFILE ($z=2.46$)

Velocity (km s ⁻¹)	[Si ⁺ /Si ³⁺]	[H ⁰ /H ⁺] _{Si}	[Al ⁺ /Al ⁺⁺]	[H ⁰ /H ⁺] _{Al}	[H ⁰ /H ⁺] _{Al + Si}
-218 < <i>v</i> < -140	1.0	-0.16	0.42	-0.06	-0.06
-140 < <i>v</i> < -110	1.7	0.12	0.47	0.00	0.12
-110 < <i>v</i> < -40	1.8	0.13	0.43	-0.04	0.13
-40 < <i>v</i> < 40	2.1	0.31	0.27	-0.30	0.31

Table 11: IONIZATION LIMITS

Note. — All values are conservative lower limits

Metal	log ₁₀ <i>N</i> (X) (cm ⁻²)	[X/H]
Fe	15.060 ± 0.024	-0.830 ± 0.051
Ni	13.628 ± 0.030	-1.002 ± 0.054
Al	SATU	
Si	15.554 ± 0.026	-0.376 ± 0.052
Cr	13.158 ± 0.030	-0.902 ± 0.064
Zn	> 12.468 ± 0.046	> -0.562 ± 0.064
C	14.616 ± 0.062	-2.324 ± 0.077
Si	14.045 ± 0.038	-1.885 ± 0.059
Pb	12.66 ± 0.114	2.23 ± 0.121
Ge	< 12.65	< 0.644

Table 12: ABUNDANCES FOR *z* = 2.462

[X/Zn]	Feature 1 -144 ↔ -110 km/s	Feature 2 -40 ↔ -9 km/s	Feature 3 -9 ↔ 35 km/s
Fe	-0.856 ± 0.185	-0.679 ± 0.175	-0.508 ± 0.243
Ni	-0.939 ± 0.204	-0.831 ± 0.186	-0.638 ± 0.249
Si	-0.388 ± 0.197	-0.157 ± 0.180	-0.035 ± 0.246
Cr	-0.833 ± 0.261	-0.729 ± 0.220	-0.534 ± 0.274

Table 13: DEPLETION RELATIVE TO Zn FOR *z* = 2.462

Metal	ΔD	$ m ^a$	$\frac{(n_H)_2}{(n_H)_1}$
Fe	0.348 ± 0.305	0.38 ± 0.05	8.2 ± 9.7
Si	0.353 ± 0.315	0.49 ± 0.15	5.3 ± 6.6
Cr	0.299 ± 0.378	0.50 ± 0.11	4.0 ± 5.3

Table 14: n_H VARIATIONS FOR $z=2.462$

^a m values are taken from Jenkins 1987

Metal	Comp 1 –211 ↔ –181	Comp 2 –181 ↔ –144	Comp 3 –144 ↔ –110	Comp 4 –110 ↔ –40	Comp 5 –40 ↔ 35
Fe	0.11	0.14	0.11	0.25	0.39
Ni	0.09	0.14	0.13	0.27	0.38
Si II	0.10	0.11	0.11	0.28	0.42
Cr	0.11	0.15	0.14	0.23	0.40
Si IV	0.17	0.46	0.09	0.14	0.10

Table 15: PERCENT OF TOTAL ABUNDANCES FOR $z = 2.462$

REFERENCES

- Anders, M.V., & Grevesse, N. 1989, *Geochim. Cosmochim. Acta*, 53, 197
- Barlow, T. 1995, in preparation.
- Bruzual, G. 1992, in *The Environment and Evolution of Galaxies* ed. J.M. Shull and H.A. Thronson, Jr. (Boston: Kluwer Academic Publishers), p.91
- Cardelli, J.A. 1994, *Science*, 265, 209.
- Evardsson, B., Anderson, J., Gutasfsson, B., Lambert, D.L., Nissen, P.E., and Tompkin, J. 1993, *Astronomy and Astrophysics*, 275, 101.
- Fall, S.M., & Pei, Y.C. 1993, *ApJ*, 402, 479
- Ferland, G. J. 1991, Ohio State Internal Report 91-01
- Field, G.B. 1975, *ApJ*, 187, 453.
- Hoffman, R.D. et al. 1995, *ApJ*, submitted
- Jenkins, E.B. 1987, in *Interstellar Processes* ed. D.J. Hollenbach and H.A. Thronson, Jr. (Boston: D. Reidel Publishing Company), p. 533
- Kulkarni, S.R., & Heiles, C. 1987, in *Interstellar Processes* ed., D.J. Hollenbach and H.A. Thronson, Jr. (Boston: D. Reidel Publishing Company), p.87
- Lanzetta, K. M., Wolfe, A. M., Turnshek, D. A., Lu, L., McMahon, R. G., & Hazard, C. 1991, *ApJS*, 77, 1
- Larimer, J.W. 1988, in *Meteorites and the Early Solar System History* ed., J.F. Kerridge and M.S. Mathews (Tucson: University of Arizona Press), p. 365
- Lu, L., Wolfe, A. M., and Turnshek, D. A., & Lanzetta, K. M. 1993, *ApJS*, 84, 1
- Lu, L., Savage, B. D., Tripp, T. M., and Meyer, D. M. 1995, *ApJ*, 447, 597
- Lu, L., Sargent, W., & Barlow, T.A. 1995, to appear in *Cosmic Abundances: The Proceedings of the 6th Annual October Astrophysical Conference in Maryland*
- Lu, L., Sargent, W., & Barlow, T.A. 1996a, in preparation
- Lu, L., Sargent, W., & Barlow, T.A. 1996b, in preparation

- Madau, P. 1992, ApJ, 335, 498
- Malaney, R.A. and Chaboyer, B. 1996, ApJ, submitted
- McKee, C.F., & Ostriker, J.P. 1977, ApJ, 218, 148
- Morton, D.C. 1991, ApJS, 77, 119
- Pettini, M., Smith, L. J., Hunstead, R. W., and King, D. L. 1994, ApJ, 426, 79
- Pettini, M. 1995, private communication
- Savage, B. D. and Sembach, K. R. 1991, ApJ, 379, 245
- Sembach, K.R., Steidel, C.C., Macke, R.J., and Meyer, D.M. 1995, ApJ, 445, L27
- Snedden, C., Gratton, R.G., & Crocker, D.A. 1991, A & A, 246, 354
- Spitzer, L., & Fitzpatrick, E.L. 1993, ApJ, 409, 299
- Spitzer, L., & Fitzpatrick, E.L. 1993, ApJ, 445, 196
- Timmes, F.X., Lauroesch, J.R., & Truran, J.W. 1995, ApJ451, 468
- Tripp, T.M., Lu, L., and Savage, B.D. 1995, ApJS, submitted.
- Truran, J.W. 1995, private communication
- Vogt, S. S. 1992, in *ESO Conf. and Workshop Proc. 40, High Resolution Spectroscopy with the VLT*, ed. M.-H. Ulrich (Garching: ESO), p. 223
- Wheeler, J.C., Sneden, C., & Truran, J.W.Jr. 1989, ARA & A, 27, 279
- Wolfe, A. M., Fan, X-M., Tytler, D., Vogt, S. S., Keane, M. J., & and Lanzetta, K. M. 1994, ApJ, 435, L101
- Wolfe, A. M., Lanzetta, K. M., Foltz, C. B., and Chaffee, F. H. 1995, ApJ, in press

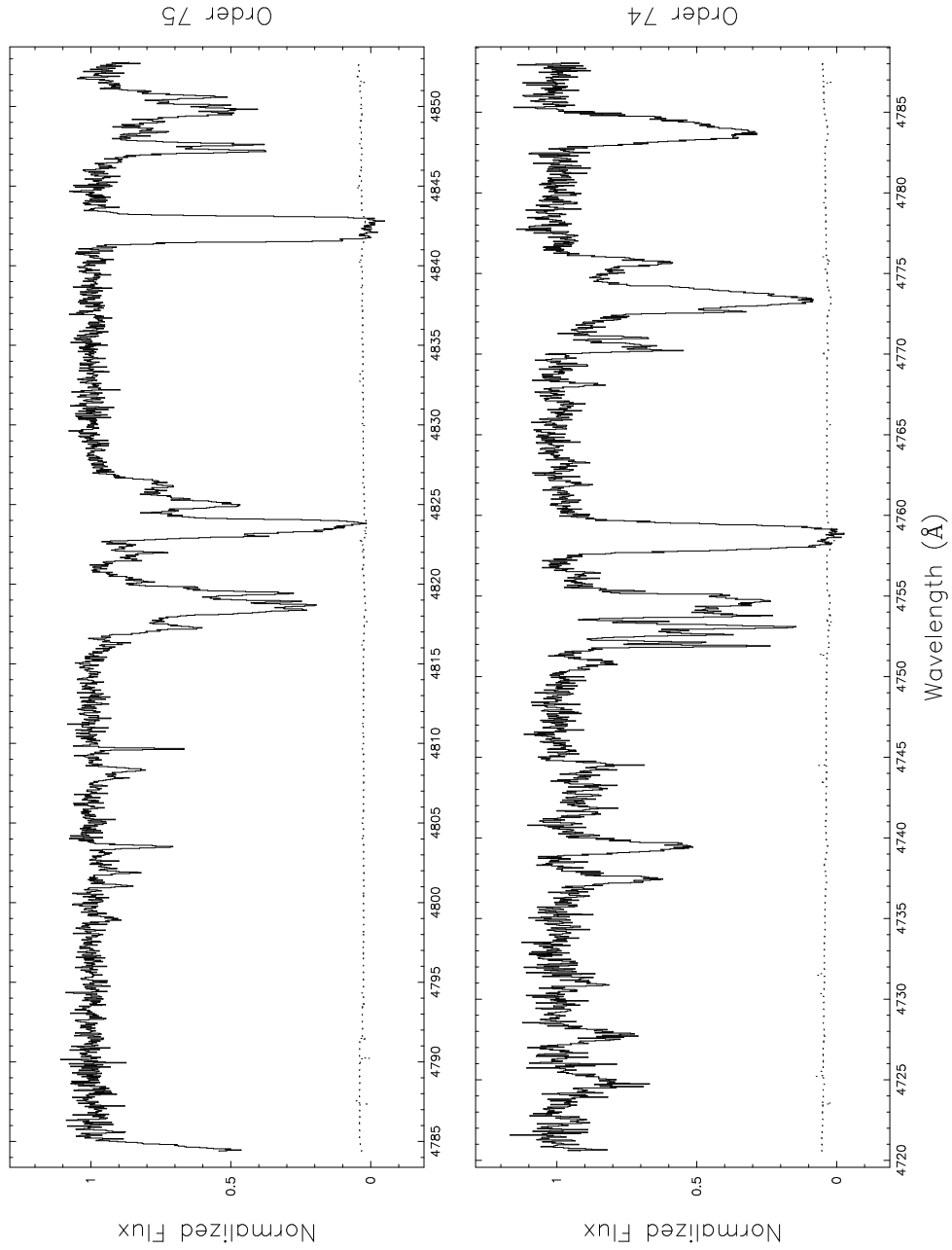


Fig. 1.— Keck HIRES spectra of Q0201+365 at a resolution of $\approx 8 \text{ km s}^{-1}$ and a SNR of ≈ 30 . All 26 orders (only 2 are shown here) are identified by the echelle order intrinsic to the Keck HIRES spectrograph. The dotted line is a 1σ error array derived assuming Poisson statistics.

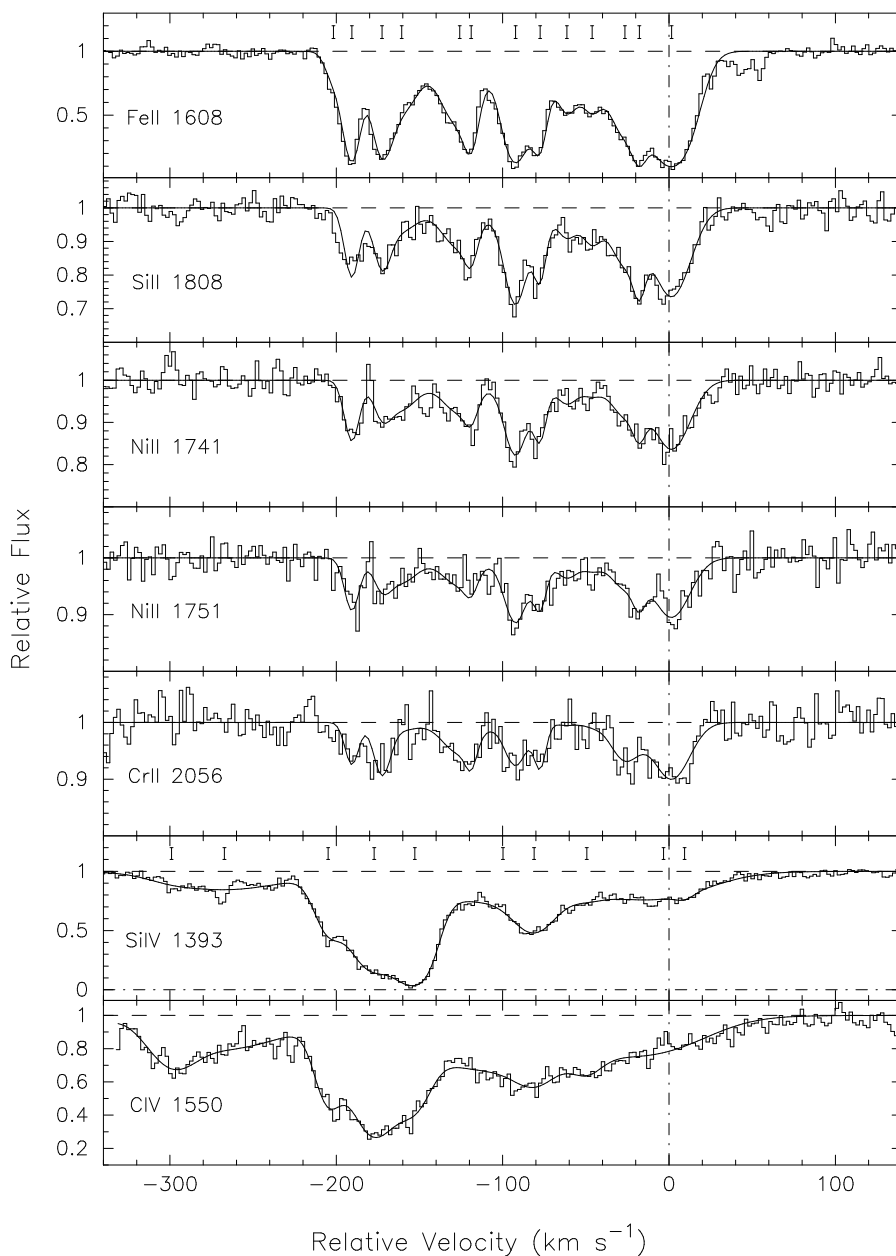


Fig. 2.— Velocity profiles of those metal-line transitions from the system at $z=2.462$ with successful VPFIT solutions. The dashed vertical line corresponds to $z=2.4628$. The marks above the Fe II 1608 and Si IV 1393 transitions indicate the velocity centroids for VPFIT solutions as listed in Table 4. In all velocity plot figures with VPFIT solutions, the leftmost mark is component 1.

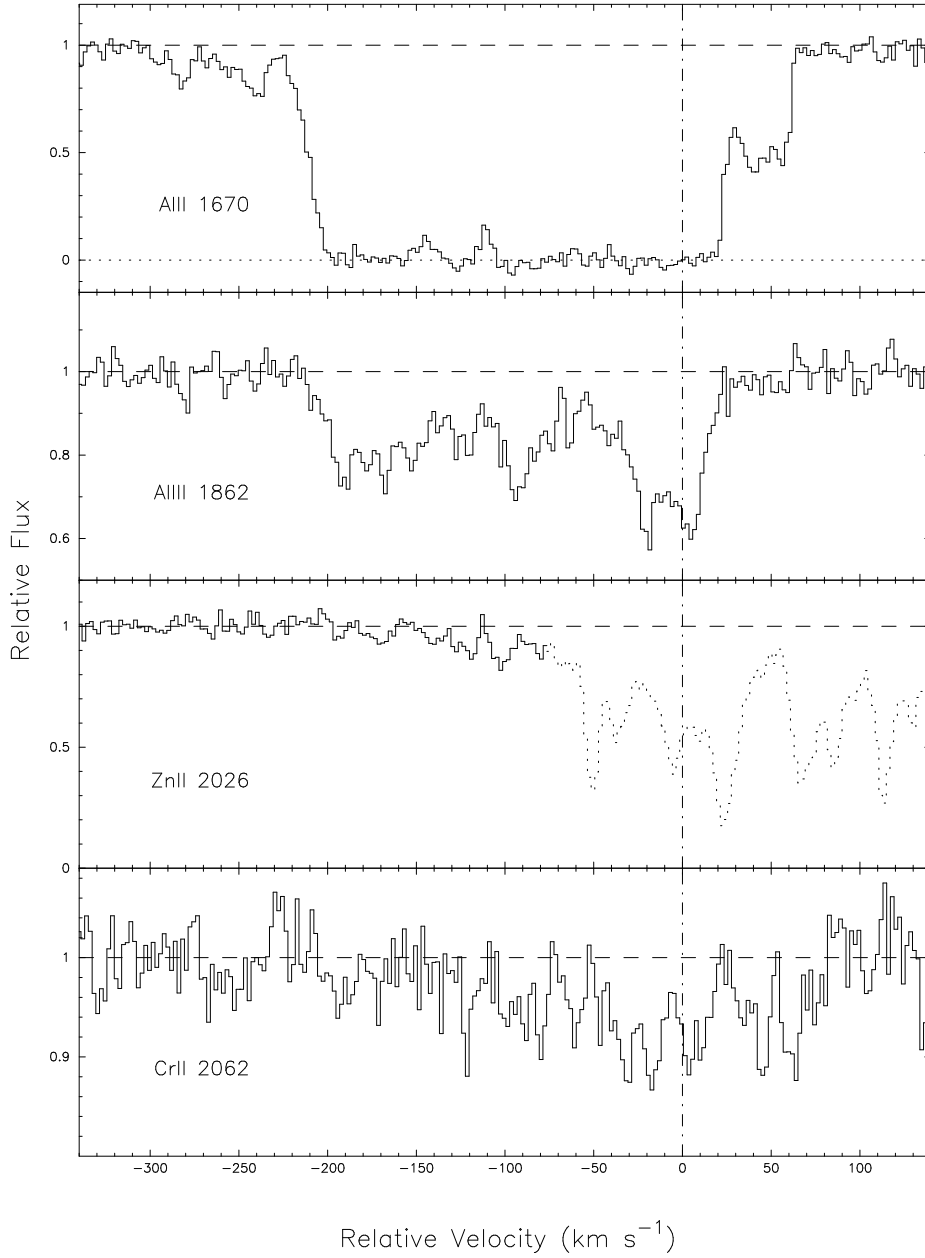


Fig. 3.— Velocity profiles of those metal-line transitions from the system at $z = 2.462$ without VPFIT solutions. The dashed vertical line corresponds to $z=2.4628$.

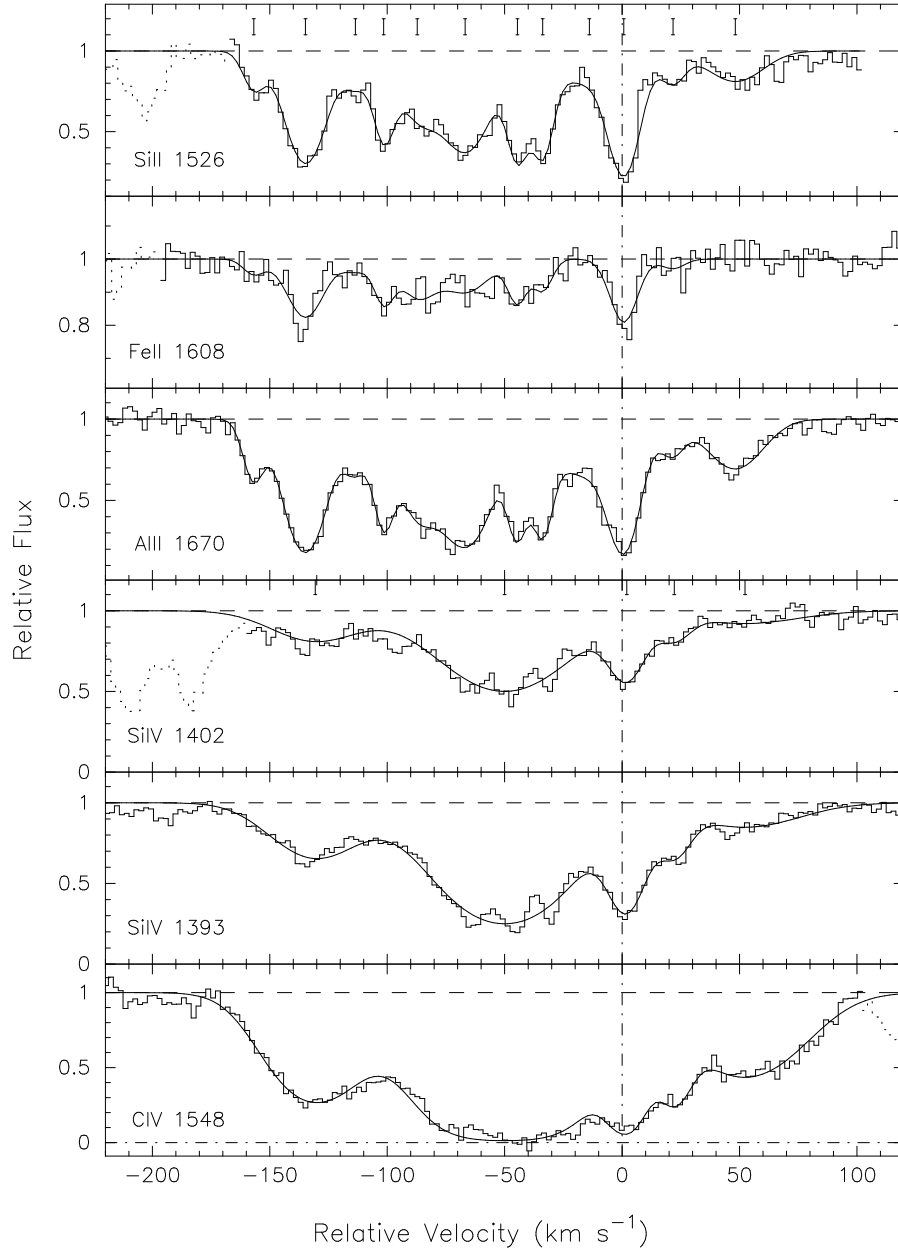


Fig. 4.— Velocity profiles and VPFIT solutions for the transitions from the system $z=2.457$. The dashed vertical line corresponds to $z=2.45785$. Those features drawn in dotted marks are due to absorption from other systems.

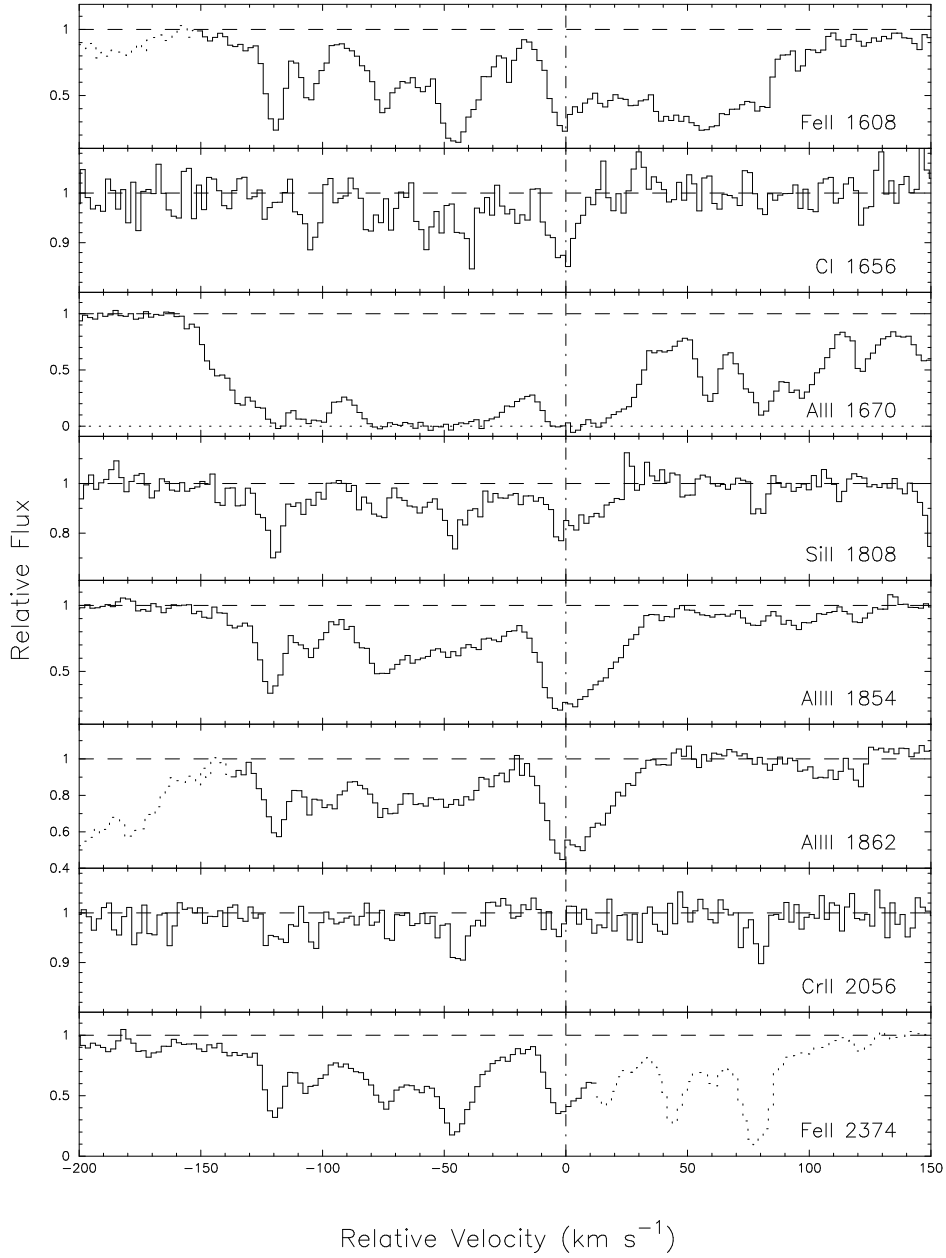


Fig. 5.— Velocity profiles for the metal-line transitions for the system at $z=1.955$. The dashed vertical line corresponds to $z=1.9555$.

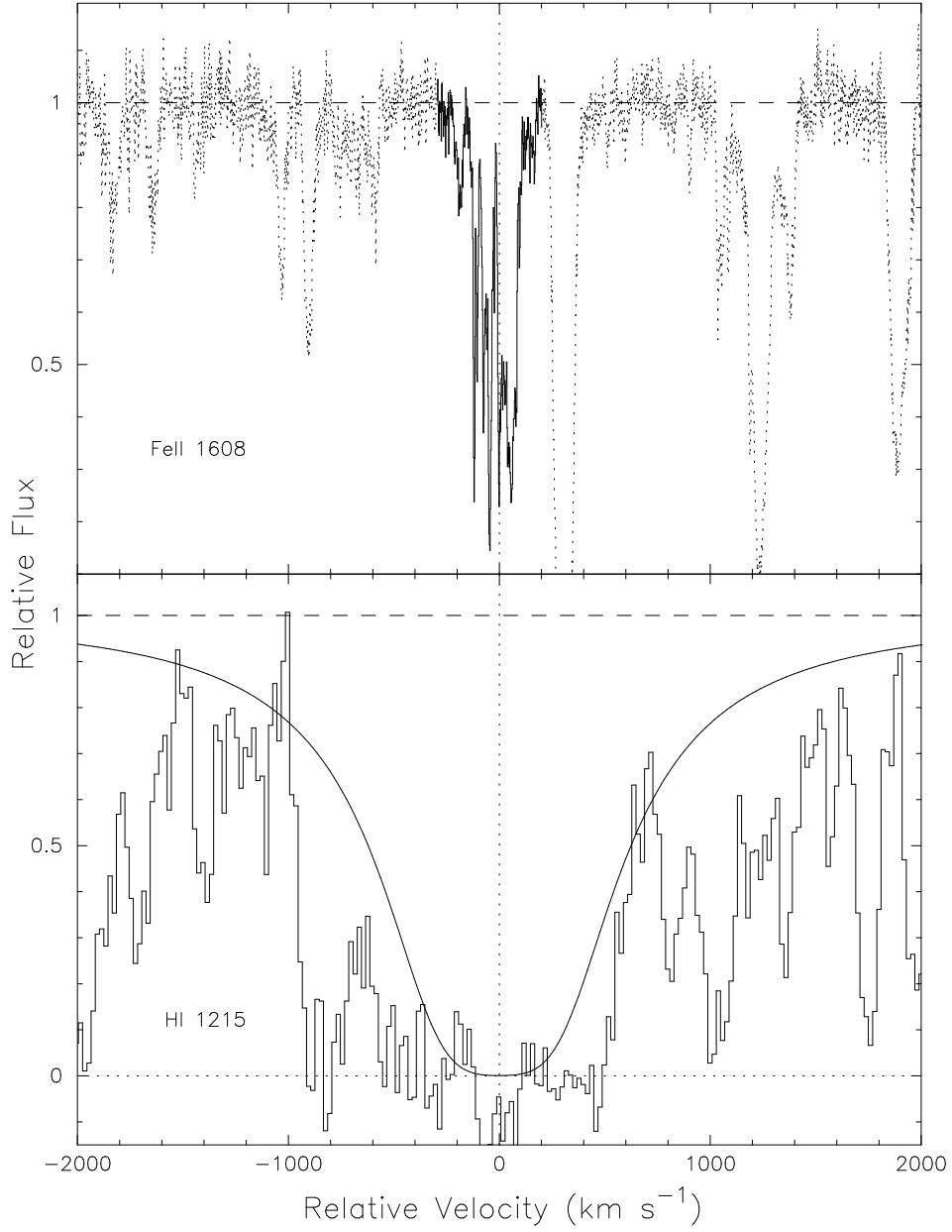


Fig. 6.— Comparison of the low-ion profile Fe II 1608 with the Ly α profile for the system at $z=1.955$. The overplotted curve in the Ly α plot is a Voigt profile corresponding to $z=1.9555$ and $N(\text{HI}) = 1.5 \times 10^{20} \text{ cm}^{-2}$.

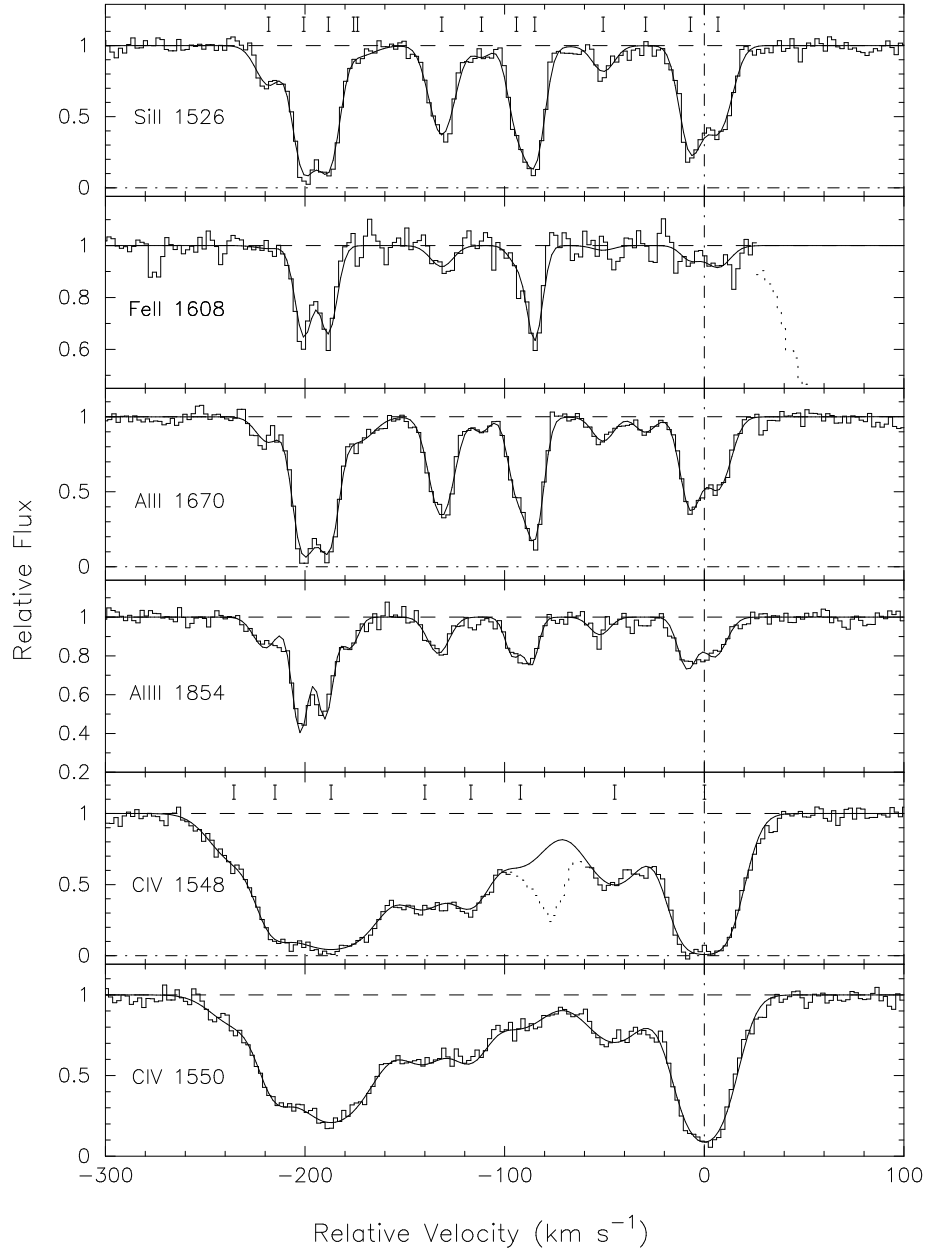


Fig. 7.— Velocity profiles and VPFIT solutions from the system at $z=2.325$. The dashed vertical line corresponds to $z=2.32612$.

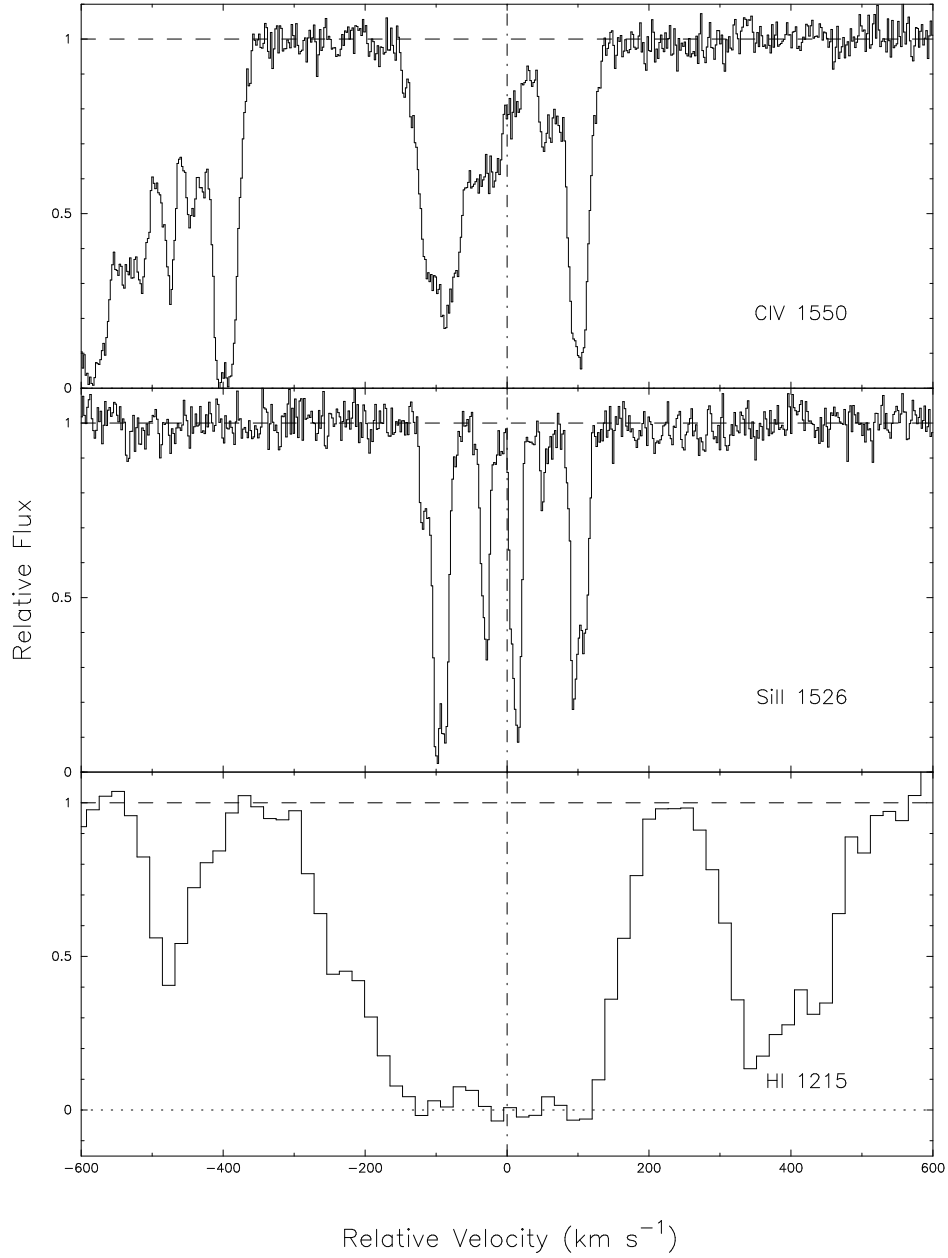


Fig. 8.— Velocity plot of the C IV 1550, Si II 1527 and Ly α transitions for the system at $z=2.325$. The transitions all span nearly the same velocity interval and appear consistent with profiles of Lyman limit systems.

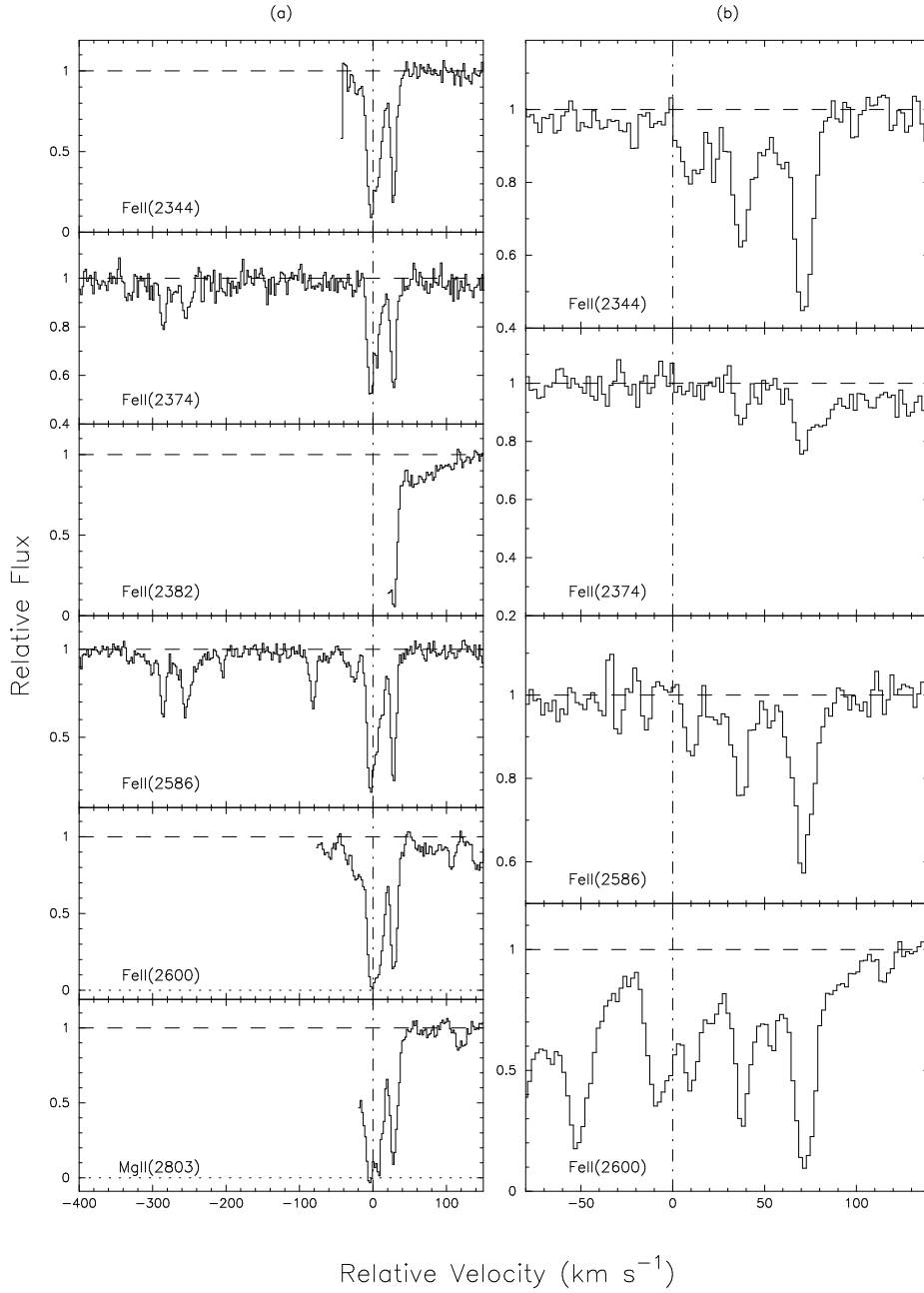


Fig. 9.— Velocity profiles of two Mg II metal systems at (a) $z=1.476$ and (b) $z=1.699$. The dashed vertical lines are at $z=1.47607$ and $z=1.699$ respectively.

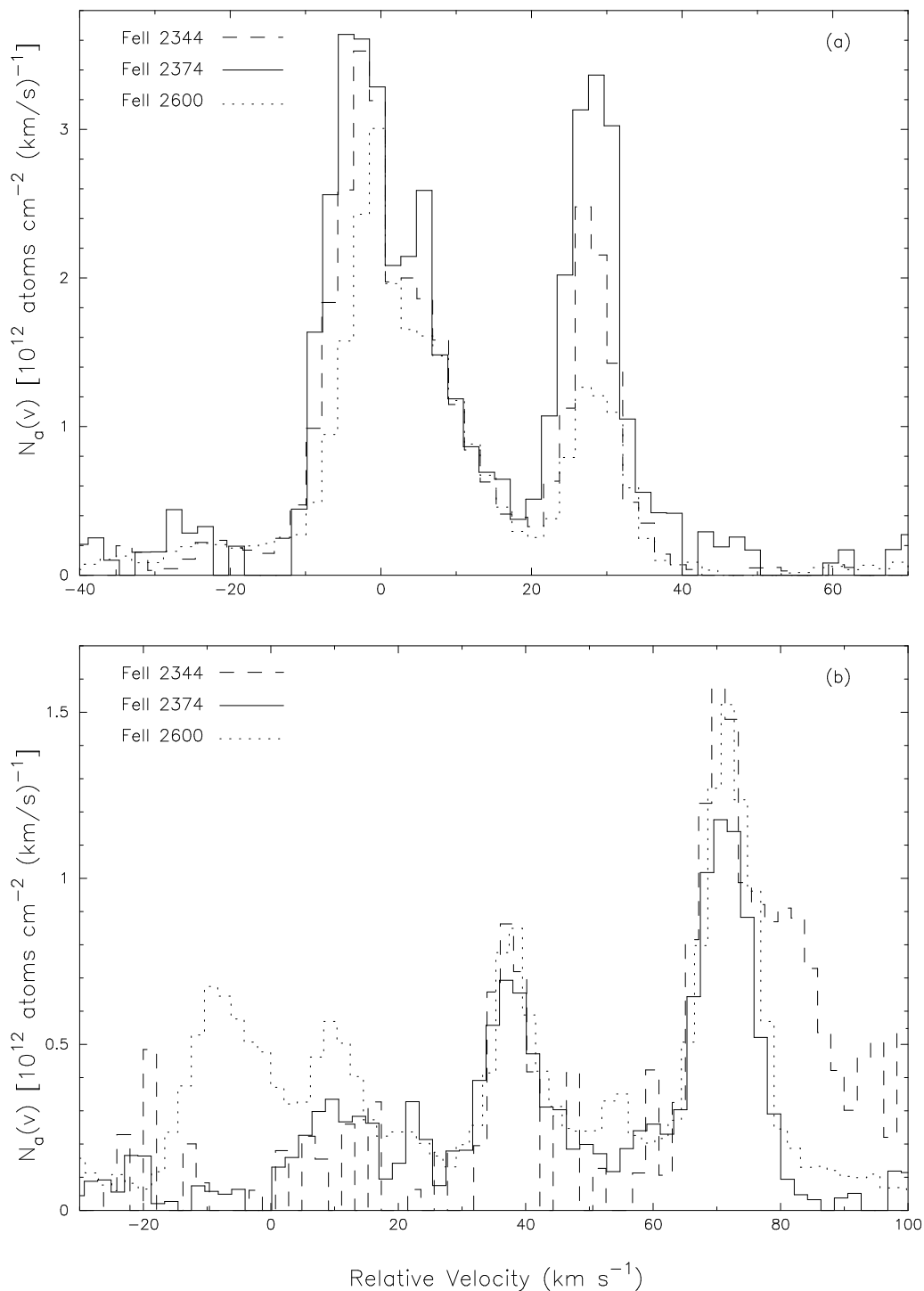


Fig. 10.— Apparent column density $[N_a(v)]$ for Fe II in the (a) $z=1.476$ and (b) $z=1.699$ systems. In (a), the regions where Fe II 2374 dominates indicate hidden saturated components. On the other hand, the features in (b) where the $N_a(v)$ profiles do not coincide are due to blends with other absorption systems.

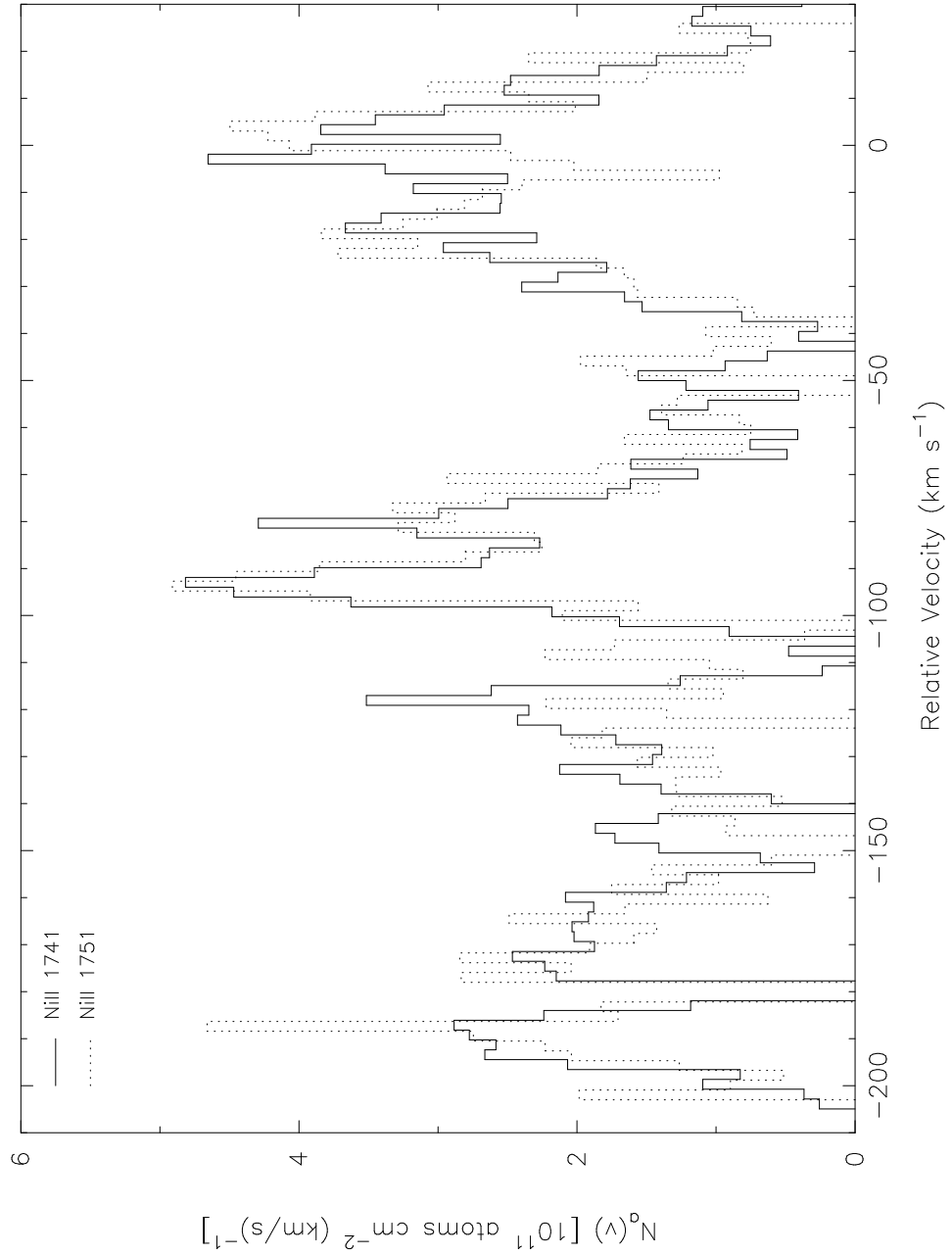


Fig. 11.— Apparent column density $[N_a(v)]$ profiles for Ni II in the $z=2.462$ system. The good agreement between the two profiles suggests there are no hidden saturated components.

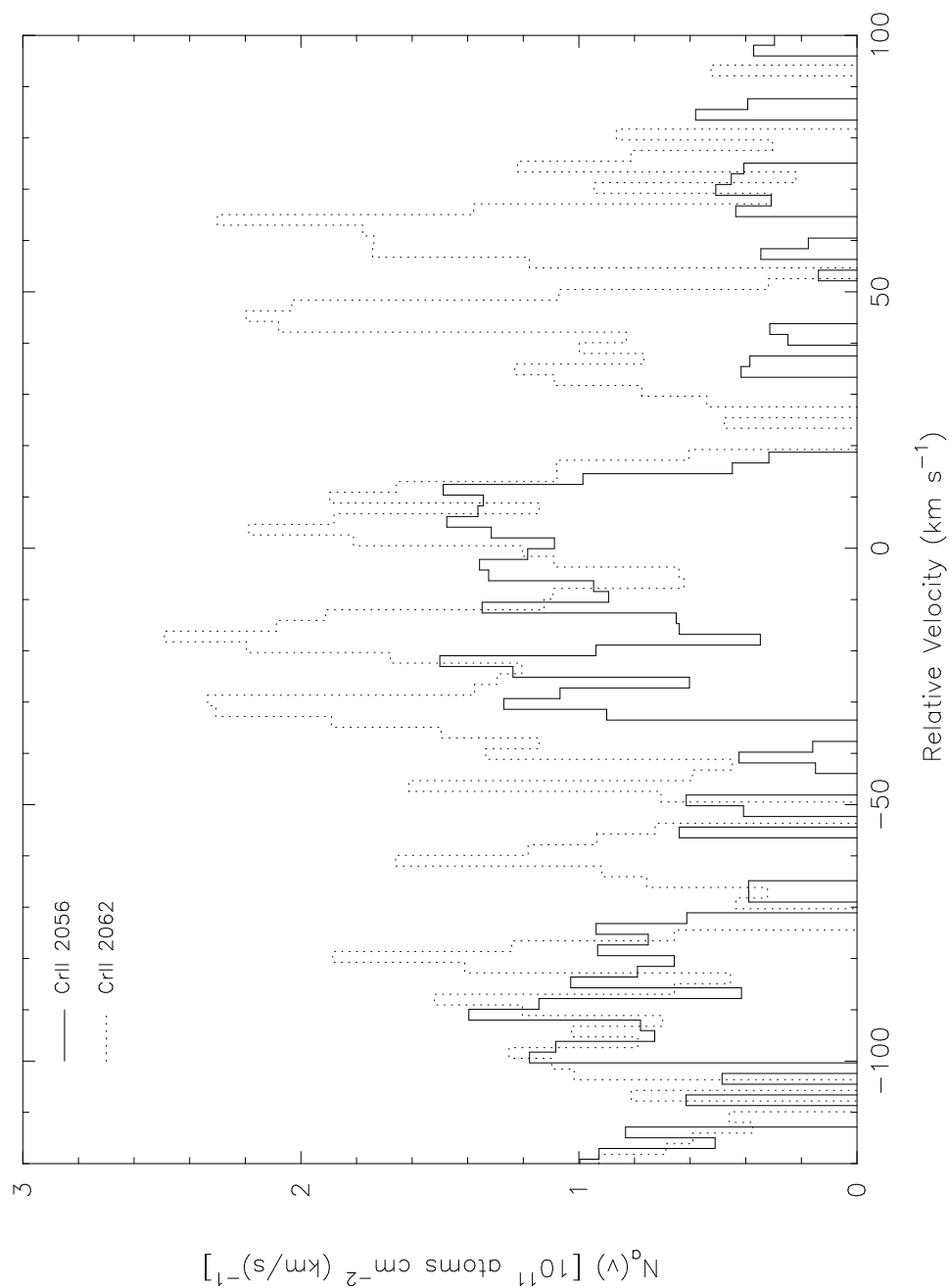


Fig. 12.— Apparent column density $[N_a(v)]$ profiles for Cr II in the $z=2.462$ system. The Cr II 2062 profile is clearly stronger over the entire velocity interval. We suggest this is due to blending in the Cr II 2062 profile by Zn II 2062. In particular, we believe the features at -60 , 40 and 60 km s^{-1} are due solely to Zn II absorption.

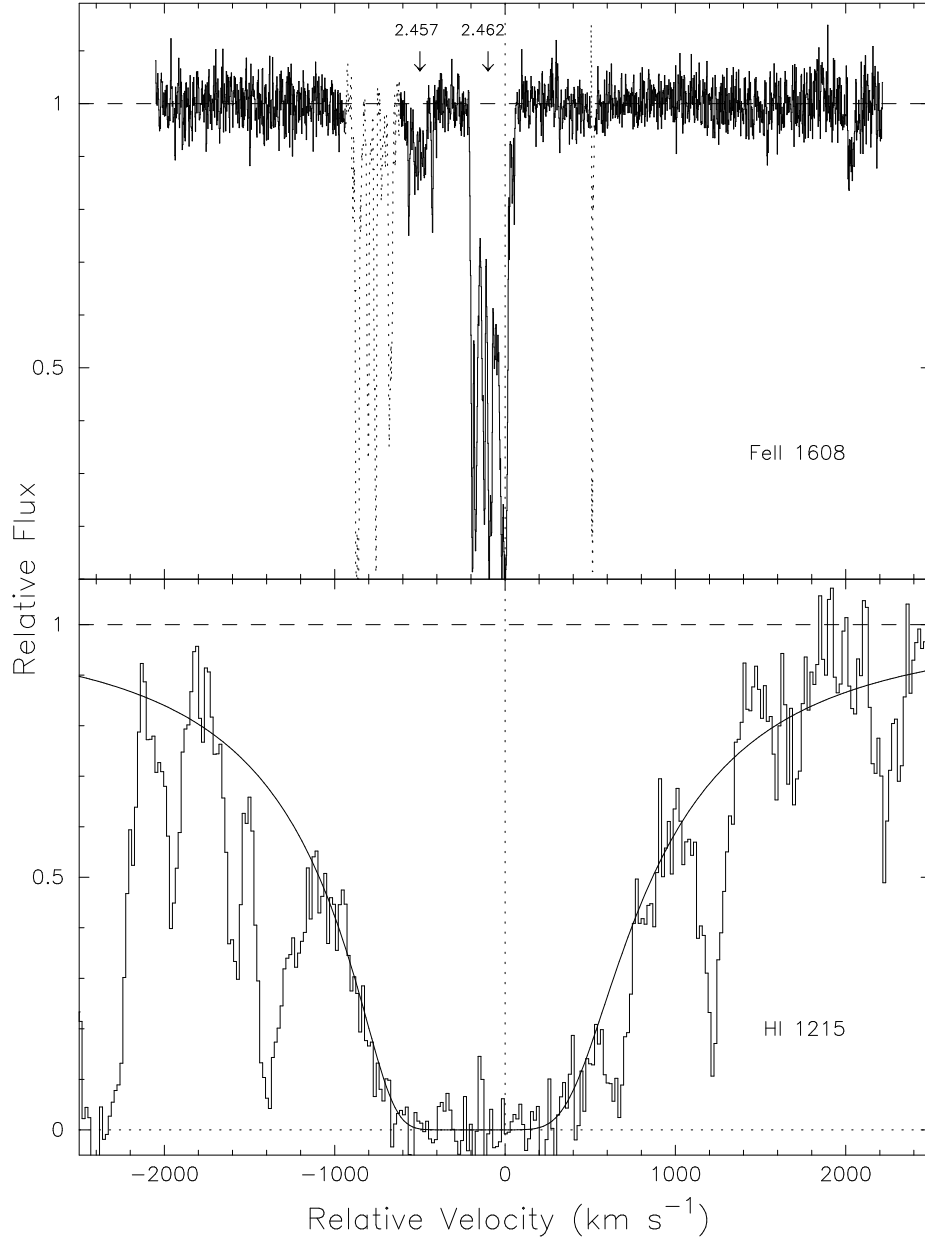


Fig. 13.— Velocity plot of the Fe II 1608 and Ly α transitions for the $z=2.457$ and $z=2.462$ systems. The Voigt profile overplotted on the Ly α velocity plot was derived with 23 individual HI components (See Table 10).

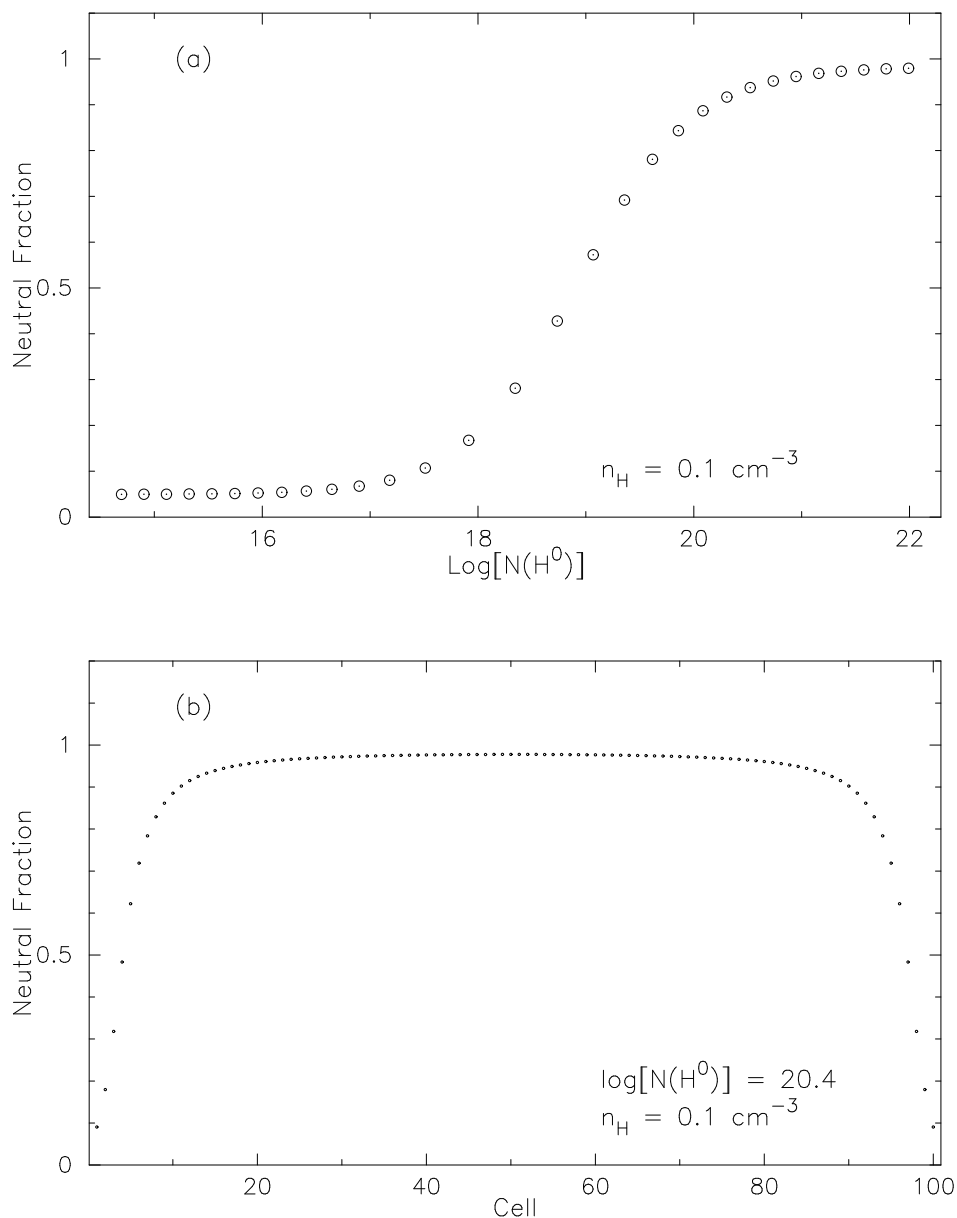


Fig. 14.— (a) Fractional ionization versus $\text{log}[N(\text{HI})]$ of a constant density ($n = 0.1 \text{ cm}^{-3}$), plane-parallel Hydrogen disk assuming a temperature of 10^4 K . The ionizing spectra is an attenuated power law spectrum, calculated by Madau (1992) at an average redshift of $z=2.46$. (b) Fractional ionization versus disk depth (expressed in cell number where cell 1 and 100 are the outer faces) for a Hydrogen system with $\text{log}[N(\text{HI})] = 20.4$. Note only the edgemost cells are significantly ionized.

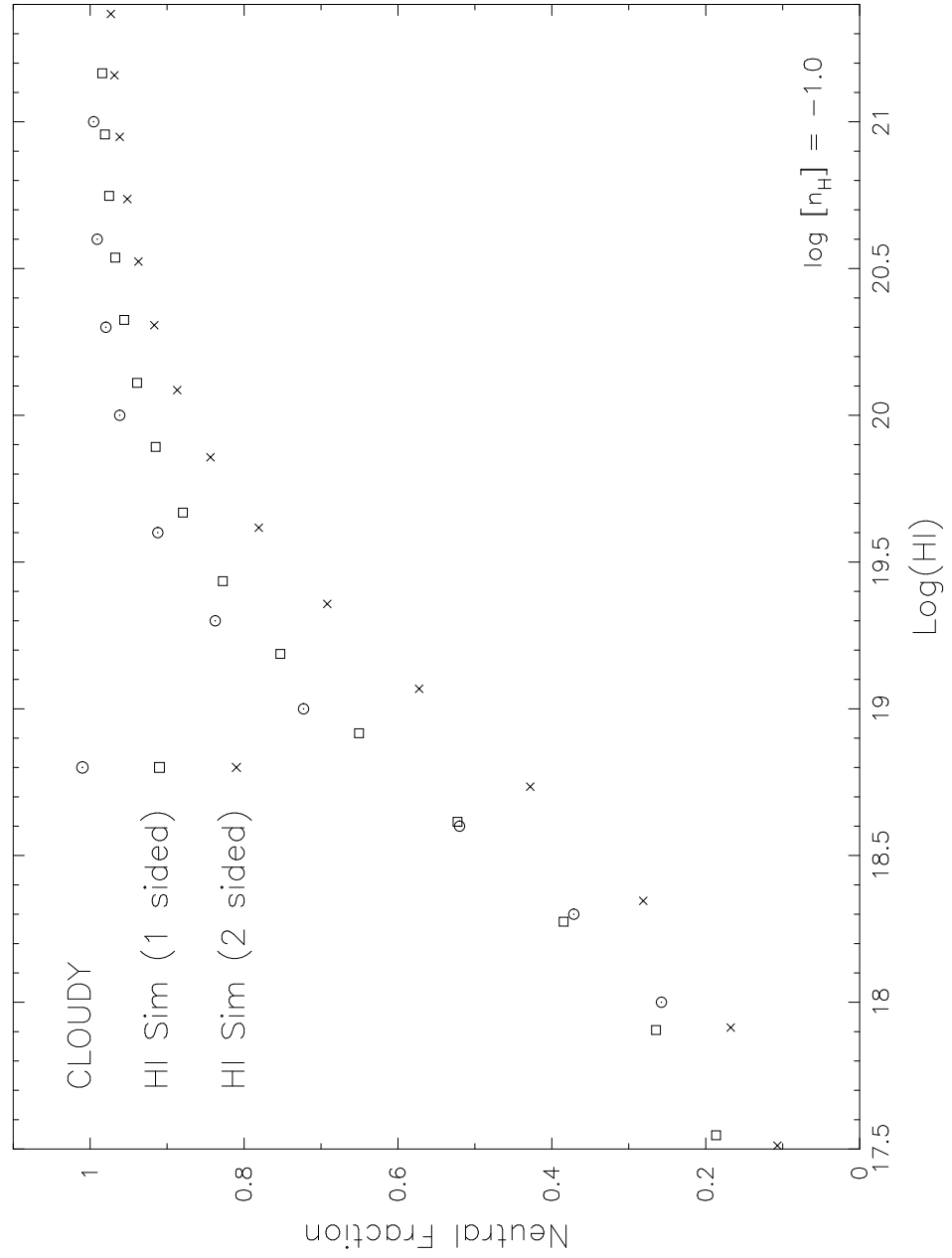


Fig. 15.— Comparison of our ionization model with CLOUDY simulations.

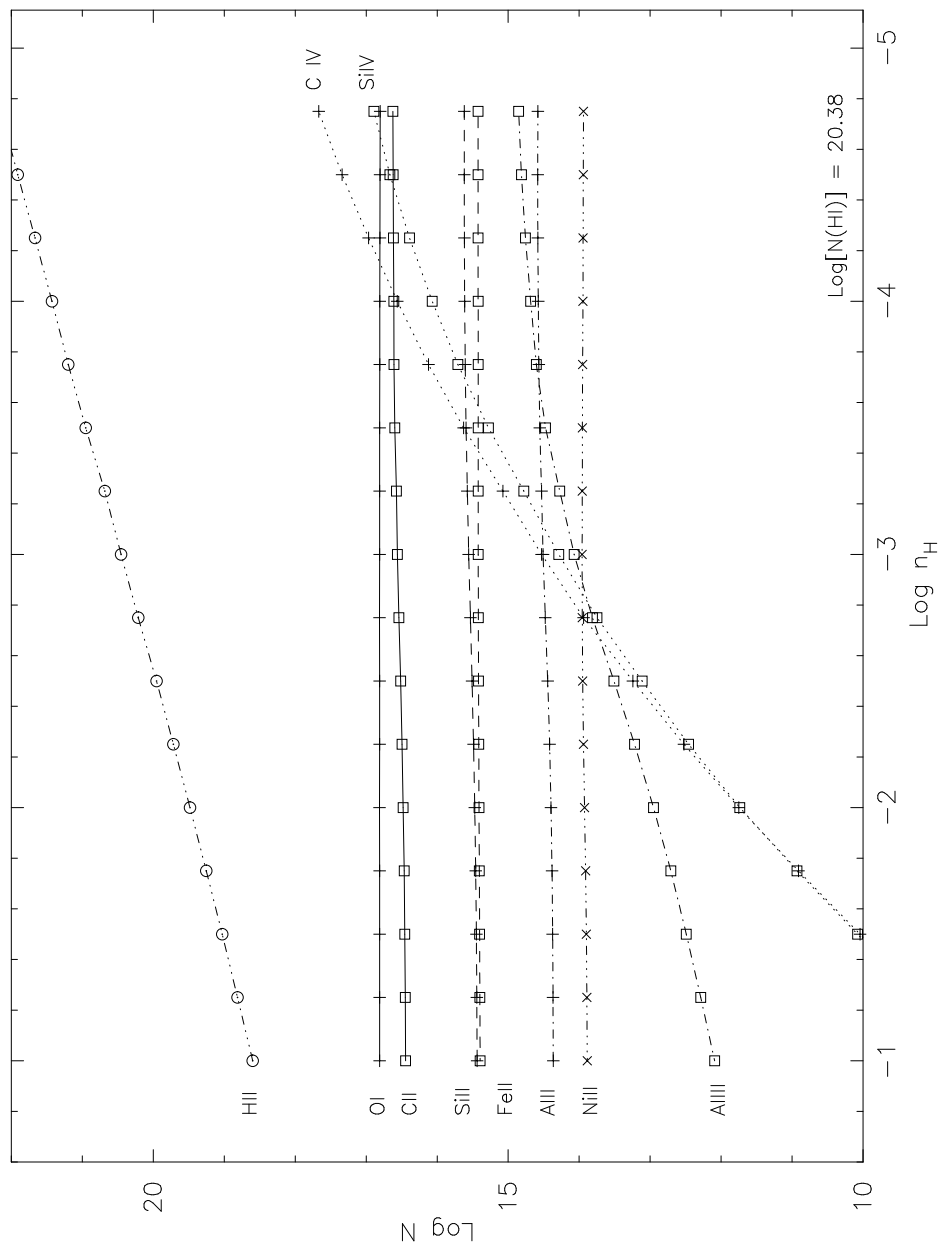


Fig. 16.— CLOUDY simulations for a series of systems with varying hydrogen volume density assuming $[Z/H] = -0.5$ and requiring $\log[N(\text{HI})] = 20.38$. The ionizing spectra is an attenuated power law spectrum, calculated by Madau (1992) at an average redshift of $z=2.46$.

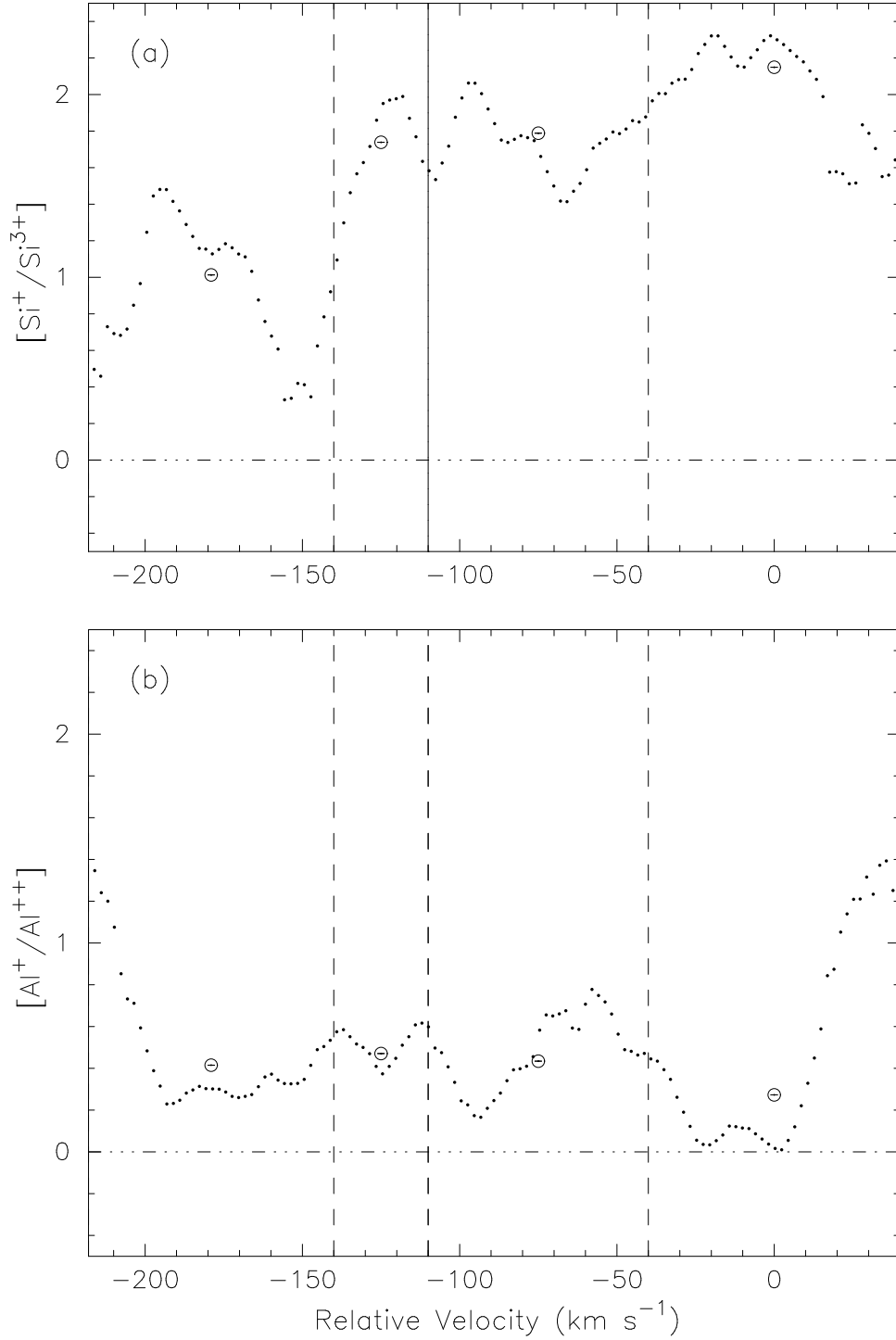


Fig. 17.— Plot of the relative logarithmic column densities of (a) Si^+ vs. Si^{3+} and (b) Al^+ vs. Al^{2+} . The $[\text{Al}^+/\text{Al}^{2+}]$ ratio was derived assuming $\log N(\text{Al}^+) = 12.0$ at each pixel and should be considered a lower limit. The two figures combined with our CLOUDY simulations further suggests that this system is predominantly neutral.

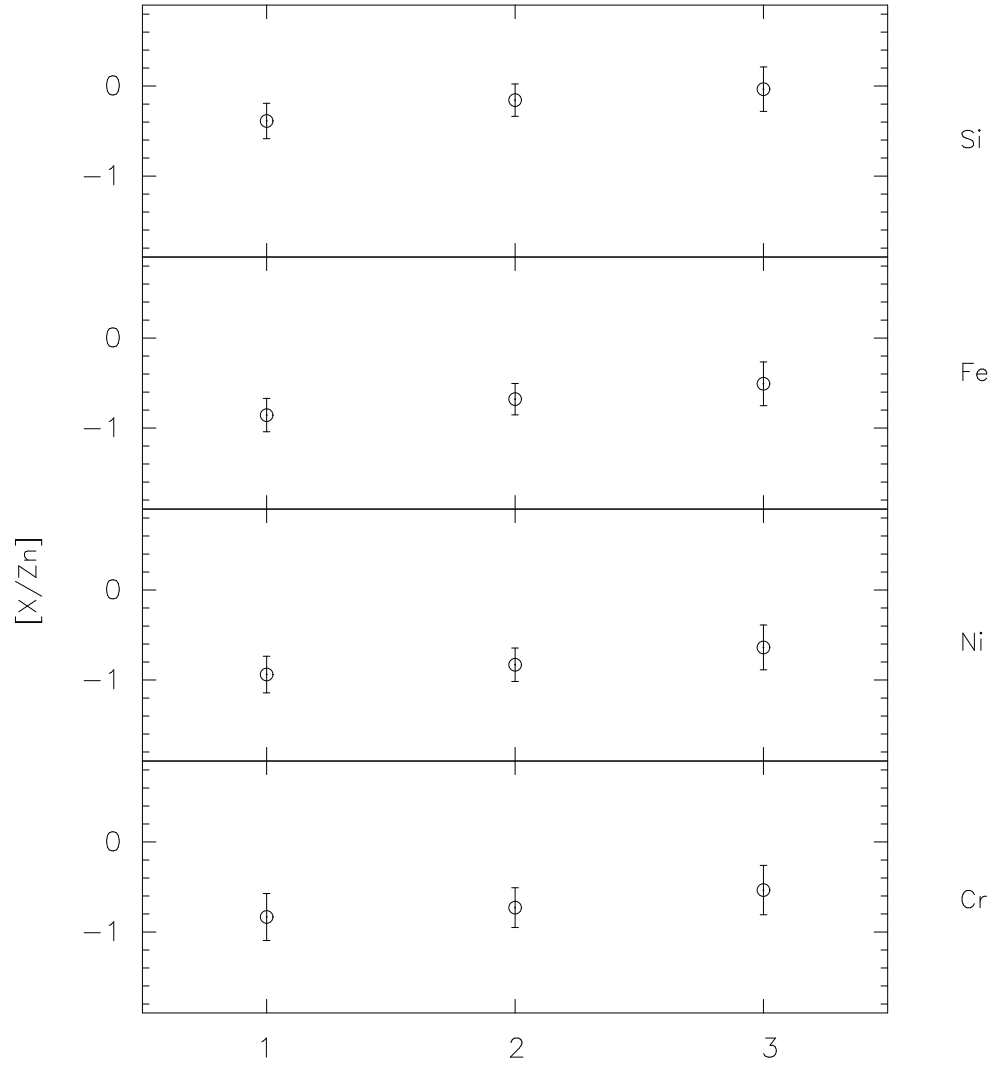


Fig. 18.— Relative cosmic abundances of Zn, Fe, Ni, Si, and Cr versus Zn for 3 velocity features of the $z=2.462$ system. Note how the relative abundances are essentially the same over all 3 features.

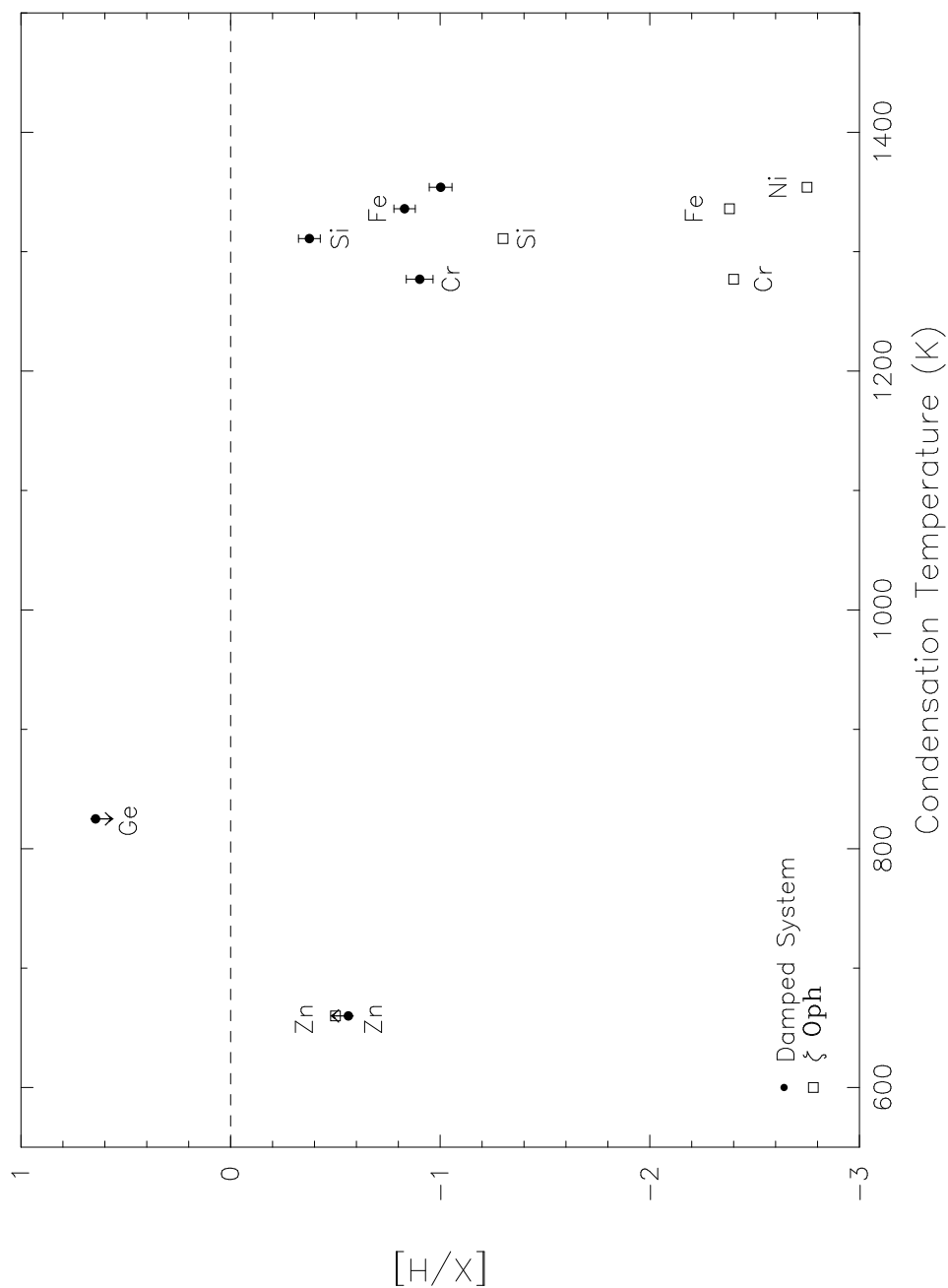


Fig. 19.— Logarithmic abundances of the low-ions Fe, Cr, Si, Ni, Zn relative to standard solar abundances versus condensation temperatures for the $z=2.462$ system (solid dots) and for the line of sight in the ISM toward ζ Oph (open squares). Note that the Zn abundance for the damped Ly α system is a lower limit whose value is most likely ≈ -0.26 .

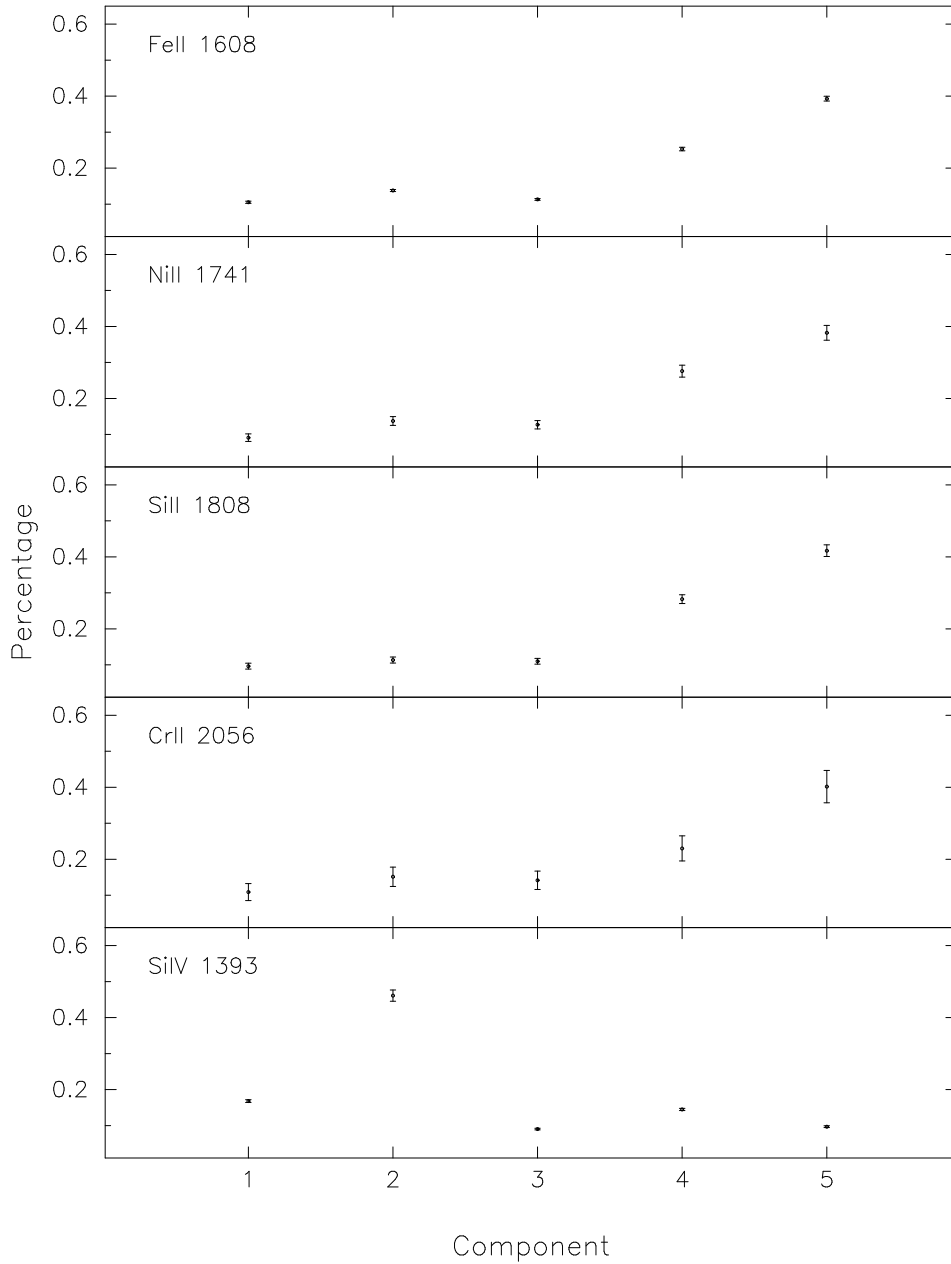


Fig. 20.— Percentage of total column densities in 5 features of the $z=2.462$ system for the Fe II, Ni II, Si II, Cr II, and Si IV transitions. Note the obvious differences between the low and high-ions. The errors were derived from the apparent optical depth method and therefore should be taken only as an approximation.